

/TWO-COLOR PYROMETER TEMPERATURE PROFILES FOR  
SINGLE PARTICLE GRAPHITE COMBUSTION/

by

Upendra Brahme

---

A MASTER'S THESIS

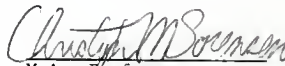
submitted in partial fulfillment of the  
requirement for the degree

MASTER OF SCIENCE

Department of Physics  
KANSAS STATE UNIVERSITY  
Manhattan, Kansas

1986

Approved by:

  
Major Professor

LD  
2668  
.T4  
1986  
B724  
c. 2

AL1206 799967

#### ACKNOWLEDGEMENTS

I approached Professors Christopher Sorensen and Fred Merklin a year ago seeking an interesting thesis topic, but they stuck me with a fascinating one. I thank them for all their support.

Special thanks go to Bill Starr for all his support inside the lab as well as the patience he demonstrated while showing me the difference between a hammer and a screwdriver. His interest and assistance made hard times bearable and good times enjoyable.

Thanks also to Everett Ramer for the guidance and helpful hints he provided.

TABLE OF CONTENTS

	<u>Page</u>
Acknowledgements. . . . .	1
List of Figures . . . . .	iii
List of Tables. . . . .	v
1. Introduction. . . . .	1
2. Background. . . . .	6
3. Experimental Design . . . . .	8
3.1 Millikan Chamber . . . . .	8
3.2 Mass Measurement and Electron Stepping . . . . .	13
3.3 Access to Burning Particle . . . . .	19
3.4 Radiation Theory and Two-Color Pyrometry . . . . .	29
3.5 Pyrometer Design . . . . .	33
3.6 Calibration of Pyrometer . . . . .	37
3.7 Pyrometer Response Time. . . . .	38
3.8 Experimental Procedure . . . . .	42
4. Results and Discussion. . . . .	43
4.1 Pyrometer Output for a Light Bulb. . . . .	43
4.2 Single Particle Traces . . . . .	43
4.3 Mean Particle Behavior . . . . .	56
4.4 Error Analysis . . . . .	68
5. Recommendation for Future Work. . . . .	71
6. Appendices. . . . .	73
6.1 Notation . . . . .	74
6.2 Computer Program . . . . .	74
6.3 Data Sheet for Pyrometer Components. . . . .	76
6.4 Pyrometer Outputs for Single Particle Graphite with Temperature Profiles . . . . .	83
7. References. . . . .	173

LIST OF FIGURES

<u>Figure</u>		<u>Page</u>
1	Exploded view of Quadrupole. . . . .	9
2	Cross Section of Quadrupole. . . . .	10
3	Circuitry for Quadrupole . . . . .	12
4	Combustion Optics. . . . .	14
5	Experimental Set-up. . . . .	15
6	Black Body Curve . . . . .	21
7	Temperature vs. Ratio of Intensity . . . . .	23
8	Effect of Bandwidth on Ratio of Intensity. . . . .	26
9a	Pyrometer Output for a Light Bulb Using 10 nm Filter . . . . .	28
9b	Pyrometer Output for a Light Bulb Using a 100 nm Filter. . . . .	28
10	Block Diagram of Pyrometer . . . . .	30
11	Analysis of Optical System . . . . .	32
12	Current Amplifier Circuit. . . . .	35
13	Pyrometer Response Time Set-up . . . . .	39
14	Pyrometer Output for Response Time . . . . .	41
15	Pyrometer Output for a 50W AC Light Bulb . . . . .	45
16	Pyrometer Output for a 30 $\mu$ m graphite Particle Heated by a Laser in Oxygen . . . . .	49
17	Pyrometer "Ringing". . . . .	51
18	Pyrometer Output for a "Suspicious" Particle . . . . .	52
19	Pyrometer Output for a "Suspicious" Particle . . . . .	53
20-25	Graphite Particles "Burning" in Air. . . . .	59
26	Graphite Particles Heated in Nitrogen. . . . .	65

<u>Figure</u>		<u>Page</u>
27	Graphite Particles heated in Oxygen. . . . .	66
28	Comparison of Peak Temperatures for Particles in Oxygen/Nitrogen . . . . .	67

LIST OF TABLES

<u>Table</u>		<u>Page</u>
1	Effect of Bandwidth on Ratio of Intensity. . . .	25
2	Time-Temperature Data Analysis . . . . .	47
3	Summary of Data. . . . .	56

## 1. INTRODUCTION

The year 1986 is likely to be recorded in the world history as the time of the greatest nuclear disaster. With the public aware that oil supplies are limited and nuclear accidents, like the one in Chernobyle, yet possible, increasing emphasis is being placed on coal utilization.

A significant amount of work has previously been done on the direct utilization of coal in boilers, formation of soot, burning of coal including temperature histories, but there is a dearth of single particle temperature and mass loss data reported in the literature.

The goal of this study was to investigate, record and correlate the temperature profiles of individual graphite particles as they burned and to determine the mass lost, as a result of laser heating.

Preliminary work was done by Joseph Cerv in 1985 and is documented in his thesis.<sup>1</sup> To give the reader some background about the importance of earlier work done in this regard, I briefly reproduce Cerv's introduction below.

Theoretically, the oxidation of carbon has been one of the most intensely considered topics in the field of combustion. Experimentally, the data on carbon combustion, especially dealing with temperature profiles and mass loss is lacking. The major studies and experiments with carbon sphere combustion are as follows.

In 1924, Nusselt<sup>2</sup> proposed his "shrinking drop" model for the combustion of a solid sphere such as wood or coal. This model

assumes that oxidation occurs only at the surface producing CO and/or CO<sub>2</sub> and that the internal temperature history is governed strictly by a one dimensional conduction equation. When a point on the sphere reaches a characteristics pyrolysis temperature, it is assumed to have burnt. While this model was a start, it failed for several reasons. It ignored temperature dependence of reaction rates, diffusion limits, and ash effects.

In 1931, Burke and Schumann assumed that pure carbon is consumed due to the reaction with CO<sub>2</sub> at the surface to form CO. The CO thus formed reacts with the surrounding oxygen at a flame sheet to form CO<sub>2</sub>. The CO<sub>2</sub> thus formed at the flame sheet then diffused back to the surface to sustain the process.

In 1951, Spalding<sup>3</sup> developed the principles of liquid drop combustion which used an evaporative vapor-phase diffusion flame to describe the combustion of droplets. While this model adequately described several solid and liquid combustion systems, it failed in the case of carbon. Due to the high sublimation temperature of carbon which is 3800° K, it does not have a significant vapor phase concentration at realistic combustion temperatures.

In 1958, Coffin<sup>4</sup> developed a system for determining the steady state burning rate of solids utilizing mass transfer coefficients rather than vapor phase diffusion. Using this method, he was able to effectively model for the cases in which the mass transfer processes are rate-determining.

The late 1970's brought expensive oil and renewed interest in coal combustion. This factor, coupled with an increase in the availability of computational facilities, spawned several computer model studies. Principle among the computer model studies was the one by Libby and Blake.<sup>5</sup> They used a computer model of a single coal particle that considered ash effects and reaction rates as well as diffusion, established the concept of extinction diameter. The extinction diameter is the particle size at which a burning particle's heat loss exceeds its heat production. At the extinction diameter the particle extinguishes itself.

Laurendeau,<sup>6</sup> in "Heterogeneous Kinetics of Coal Char Gasification and Combustion", covered all aspects of the topic: coal and char characteristics, surface mechanisms, particle reaction models, and kinetics of char gasification and combustion. Of principle interest in this study is the comparison of the Shrinking Drop Model, which strictly assumes a surface reaction, to the Progressive Conversion Model, which considers pore effects. For small particles on the order of tens of microns, there is considerable question as to which is the proper mechanism.

Experimentally, the literature is sparse. In the 1930's studies were done by Tu, Hottel and Davis<sup>7</sup> to determine the combustion rate of carbon. Large spheres (2.5 cm in diameter) and carbon samples in cups were heated in furnaces, the mass loss rates were measured and the gas profiles around the carbon bodies were sampled. These experiments validated Burke and Schumann's idea of

the flame front for large particles. However, it must be remembered that this work was conducted with large particles.

Experimental work in the area of individual coal particle combustion slowed in the 1940's as pulverized coal began being used as a fuel in boilers. Interest shifted to furnace design with large groups of interacting particles. Sherman in 1940 analyzed the space requirement for pulverized fuel combustion using an entrained flow of coal particles through a furnace. Even though data was needed on individual small particles, it was not until 1976 that work in this area was conducted.

In 1976, Ubhayaker and Williams<sup>8</sup> studied the burning rate of small carbon particles (50  $\mu\text{m}$  - 200  $\mu\text{m}$ ). The particles were suspended on a quartz fiber with grease and ignited with a pulse from a ruby laser. As the particle ignited, it fell from the quartz fiber and was followed by a high speed camera. Additionally, two color pyrometry gave a temperature history. Results showed that for 40-200  $\mu\text{m}$  particles the flame sheet idea is not valid and the flame is confined to the particle surface. Additionally, particle extinction was experimentally verified.

Since the study by Ubhayaker, high speed cinematography and two color pyrometry have been used in several studies that follow particles through a furnace. This system gives burnout times and temperature histories for 50-100  $\mu\text{m}$  particles.

Real boilers use fuel sieved through 200 (74  $\mu\text{m}$ ) or 400 (37  $\mu\text{m}$ ) meshes. This gives a size distribution weighted in the 20-50  $\mu\text{m}$  range. Studies have not been conducted on these sized carbon

particles because up to now, there has not been an experimental method by which they could be measured. In the past 15 years a new version of an old device, the modified Millikan cell, has been developed that can isolate, hold, and weigh these size particles.

The bihyperboidal Millikan cell was first developed in 1970 at Aberdeen Proving Ground to provide a method for isolating and observing 20 to 100 um aerosol particles.<sup>9</sup> In 1981, Arnold<sup>10</sup> developed the concept of electron stepping as a method of mass and charge measurement. This concept is based upon the fact that if a charged particle lost an electron, the particle mass and charge can be determined from two voltage measurements. Arnold applied this concept to a flat plate Millikan cell and was able to weigh picogram size particles. In 1982, Philip, et al., showed that the technique of electron stepping could also be used in the bihyperboidal Millikan cell and an extremely sensitive mass isolation and measuring device was available.<sup>11</sup> It has the capability of capturing and holding a particle at one position in space and it can weigh particles in a mass range from  $10^{-9}$  g to  $10^{-12}$  g. Since 1981, the modified Millikan cell has been a piece of equipment in search of a use.

## 2. BACKGROUND

The development of the two-color optical pyrometer is attributed to Hottel and Broughton.<sup>12</sup> They used the pyrometer to measure true temperature and total radiation of luminous flames. The two-color pyrometer measures brightness temperature at two different, but known wavelengths; substitution into Planck's law yields two simultaneous equations which yield the true temperature.

In 1961, D. Rae used the two-color method to determine the temperature of frictional sparks. Rae noted that sensitivity of the system is greatest when

$$\left( \frac{1}{\lambda_A} - \frac{1}{\lambda_B} \right) = \frac{2T}{C_2} \quad (1)$$

and he chose his photocells accordingly.  $\lambda_i$  are the effective wavelengths of the detectors, and  $C_2$  is a constant that will be defined later. Measurements were made in excess of 4000° K. Rae also used his intensity measurements to detect explosion of Titanium particles.

In 1972, Ayling and Smith<sup>16</sup> burned pulverized fuel particles in a plug flow reactor that had several ports for optical access. They used a single photomultiplier with rotating filters to view the stream of particles passing by a single port.

Ubhayaker and Williams<sup>8</sup> were the first to apply the two-color pyrometer to singly burning particles. They suspended electrode carbon particles in oil droplets on the end of a thread and ignited them with a laser. House<sup>13</sup> at MIT measured temperatures of coal

particles as they flowed past an optics probe inserted up to the bottom of a quartz laminar flow furnace. Dictor<sup>14</sup> extended House's work to enable determination of complete temperature profiles from particle ignition to extinction. Both House and Dictor used a light pipe to collect, split and guide the light to narrow bandwidth detectors. Signals from the detectors were displayed on a memory oscilloscope, photographed and measured by hand to enable temperature calculation. This study is an extension of the previous work done by Joseph Cerv in the sense that particle temperature data is also incorporated.

### 3. EXPERIMENTAL DESIGN

To enable temperature measurements, a graphite particle must be "isolated"; the light from the burning particle must be collected, split, led to detectors, amplified, measured and recorded. Additionally, the system requires calibration, and the raw data needs to be converted to actual temperatures. The procedure to accomplish this task is described here.

#### 3.1 Millikan Cell

The equipment and technique for mass determination followed as closely as possible to that of Philip.<sup>11</sup> The quadrupole (Modified Millikan Cell) shown in Figs. 1 and 2 that suspends the particles has surfaces defined by the following equations. The inner surfaces of the endcap electrodes are given by

$$z^2 = \frac{r^2}{2} + z_0^2, \quad (2)$$

where  $z_0 = 4\text{mm}$  and is the vertical distance from the geometric center of the chamber to the endcap electrodes and  $r$  is the radial distance from the axis of symmetry. The characteristic dimension of the chamber is  $Z_0$ , half the distance between the two endcap electrodes, measured along the axis of symmetry. The inner surface of the ring electrodes is described by

$$z^2 = \frac{r^2}{2} - z_0^2. \quad (3)$$

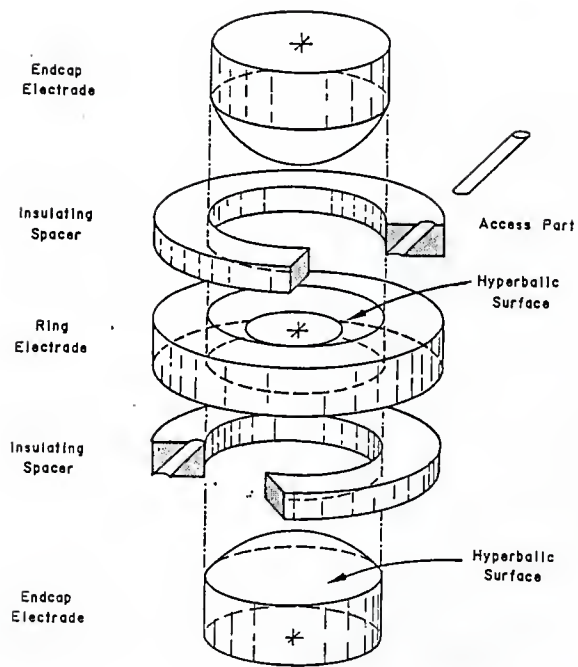


Fig. 1 Exploded view of Quadrupole

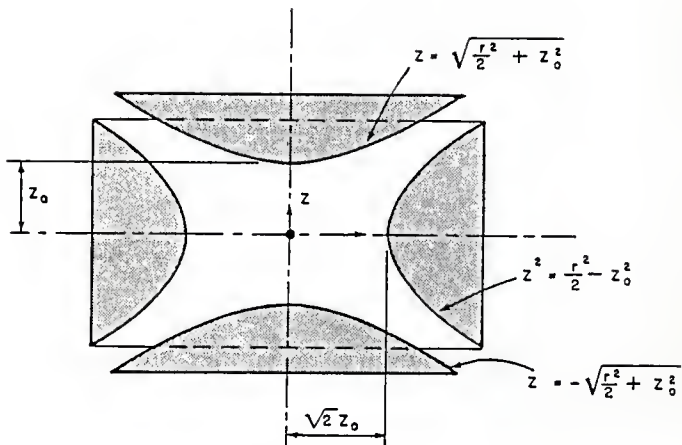


Fig. 2 Cross-section of Quadrupole

The quadrupole with insulating spacers used in this study was made by Tempco Corporation, Danvers, Mass.

The chamber consisted of a central ring electrode of aluminum and two teflon rings on either side. The two aluminum endcap electrodes were mounted in the teflon rings. Ten (1/8") access ports were drilled into the teflon ring and endcap electrodes. All access ports could be sealed by flat glass windows when not in use. All outside metal surfaces on the quadrupole were covered with teflon shields to prevent electrical shock.

The circuitry to produce the AC voltage (with DC bias) on the ring electrode and the DC voltage across the endcaps is given in Fig. 3. The capacitor-resistor network suppresses induced AC voltages on the endcap electrode resulting from the AC voltage on the ring electrode. The regulated dc power supply to produce  $V_g$  across the end cap consists of a Pacific Instruments 7104 PC card. This card is capable of producing 0-2000 V across the end caps with a resolution of 0.0005 V. The power transformers were Essex Stancor P-8151 2400 VAC CRP transformers. The power transformers were controlled by a Powerstat T/16 nongrounded variable transformer. The ring electrode system provided an rms ac voltage of 0 to 4800 V at 60 Hz with a resolution of about 50 V. Measurements of  $V_g$  were made with a Keithly 192 digital multimeter capable of reading up to  $6\frac{1}{2}$  digits. The meter was protected by a 30 A fuse on the negative lead.

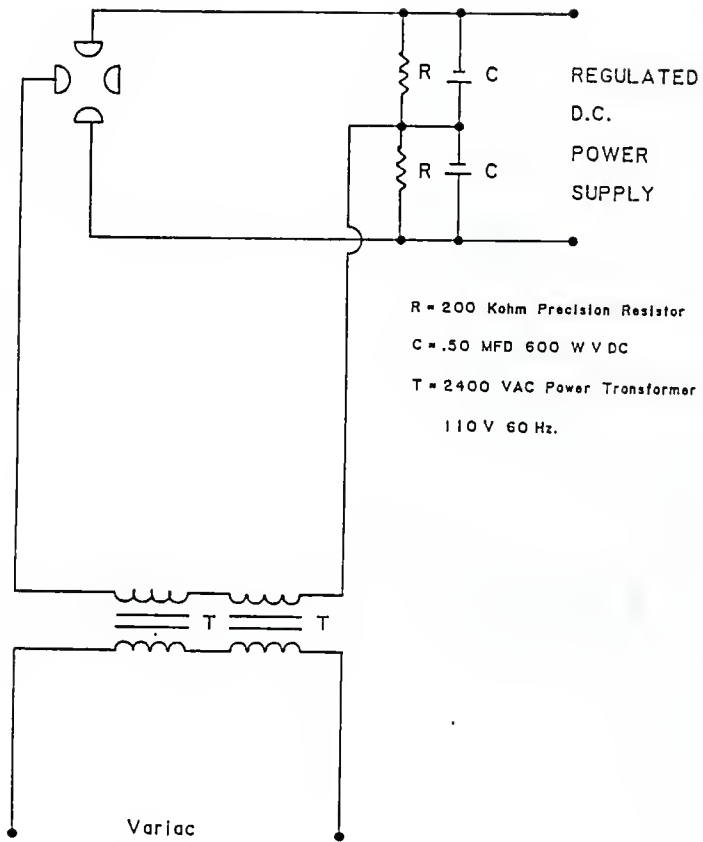


Fig. 3 Circuitry for Quadrupole

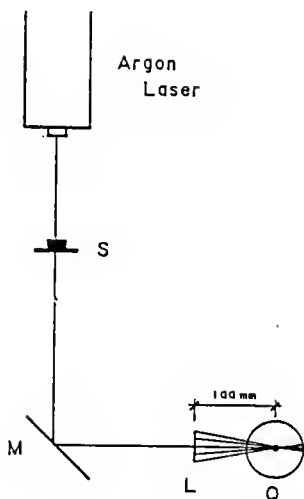
### 3.2 MASS MEASUREMENT AND ELECTRON STEPPING

The schematic of the apparatus for mass measurement and combustion optics is shown in Figs. 4 and 5, respectively.

A charged particle is levitated between a set of hyperbolic electrodes, the schematic diagram of which is shown in Fig. 2. There are two endcap electrodes between which a DC potential is applied, as well as a ring electrode to which an AC voltage is applied. The DC potential across the endcaps balances the particle against gravity, while the AC voltage on the ring provides for the focussing of the particle towards the center of the chamber. The particle is illuminated by a HeNe laser beam that traverses the chamber through ports drilled into the center of the endcap electrodes. As shown, the scattered light from the particle is observed through ports in the endcap electrode at  $23^\circ$  to the HeNe beam.

At the geometric center of the device there is no AC field. Therefore when the electric force produced by the DC field just balances the gravitational force on the particle, the center of the chamber becomes a stable equilibrium point for the particle. Stated differently, whenever a balanced particle drifts away from the center it "feels" a net force towards the center of the chamber.

Experimentally, the mass is measured as follows. The ring voltage is initially adjusted to about 500 V. The voltage across the endcaps was set to its minimum value, typically about 0.015 V. Particles were injected into the chamber with a hypodermic needle. Due to the applied AC field in the ring electrode, this often leaves several charged particles stably oscillating in the quadrupole.



Argon  
Laser

Beam Wavelength = 514.5  
Beam Power = 1 watt  
Beam Waist = .625 mm

$$w_0 = \frac{\lambda}{\pi} \frac{f}{w_l} = 2.62 \times 10^{-5} \text{ m}$$

- M - Mirror
- L - 100 mm Lens
- S - Shutter
- Q - Quadrupole

Fig. 4 Combustion Optics

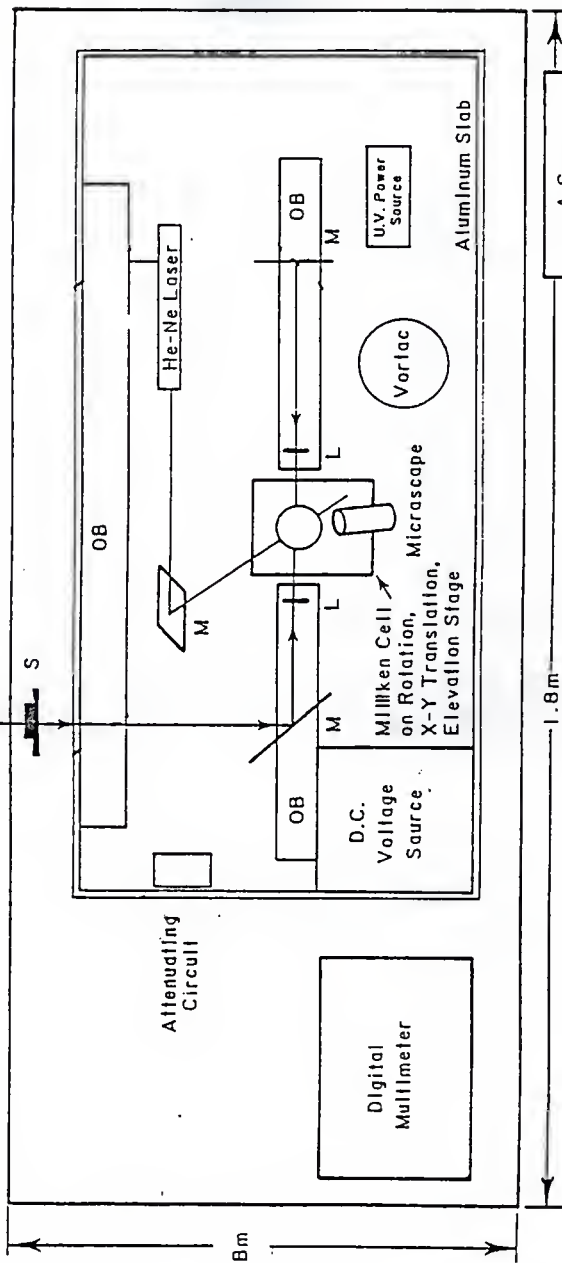
OB - Optical Bench

L - 100 mm Lens

S - Shutter

Argon Laser Beam In

M - Mirror



Experimental Schematic

Fig. 5

Then a particle that responded suitably to the balancing DC voltage was balanced at the center of the chamber. A stationary particle was assumed to be balanced since any departure from the center of the chamber resulted in oscillations of the particle. The ring AC voltage was then lowered for a few seconds. This usually allowed the unbalanced particles to fall out of the chamber while the balanced particle remained near the chamber center. The AC voltage was then increased again. The remaining particle was more carefully balanced by adjusting  $V_g$  and then lowering the AC voltage for a couple of seconds. If the particle drifted from the chamber center, it was clearly unbalanced. The ring voltage was then increased again and  $V_g$  further adjusted, after which the procedure was repeated, until, on lowering and raising the AC voltage the particle remained stable, which is recorded. The UV light was then turned on for an instant. Electron loss was verified by lowering the AC voltage and observing particle drift. The particle was then rebalanced at the chamber center by the technique already described and  $V_g$  recorded again. This procedure is repeated a number of times and from several measurements of  $V_g$  the mass and charge of the particle can be calculated.

### 3.2.1 Mass Calculation

For a stationary particle at the center of the quadrupole, a simple force balance describes the mass of the particle as

$$mg = qE$$

where E is the electric field. But for the modified Millikan cell its value is  $C V_g / Z_o$ .

q is particle charge

C is the geometric constant for the chamber equal to 0.4

g is the gravitational constant

Z is the characteristic dimension of the quadrupole  $Z_o = 4\text{mm}$

and  $V_g$  is the potential difference across the endcaps.

The charge on the particle equals the number of excess electrons times the charge on an electron, so

$$m = \frac{C n e V_g}{g Z_o} . \quad (4)$$

Collecting constants

$$m = k n V,$$

$$\text{where } K = C e / g Z_o = 1.6356 \times 10^{-15} \text{ g/V}.$$

If  $V_{n+1}$  and  $V_n$  represent the balancing voltages for a particle containing n and n+1 excess electrons, respectively, then by solving the previous equation at each balancing voltage the particle mass is given by

$$m = \frac{K V_n V_{n+1}}{V_n - V_{n+1}} . \quad (5)$$

For relatively large particles ( $10^{-8}$ ) with large numbers of excess electrons ( $10^5$ ) over a small range of voltage (1v) this can be approximated as

$$m = \frac{K V_g^2}{\Delta V \text{ for a single electron}} \cdot \quad (6)$$

The problem is now reduced to finding the voltage change for a single electron.

### 3.2.2 Measurement of $V_g$

There are two methods used to measure  $V_g$ . The first method is to capture a particle in the center of the chamber and manually adjust  $V_g$  until the particle does not oscillate. The AC voltage is turned down and the direction of the drift is noted. The AC field is turned alternately up and down and  $V_g$  is adjusted until the particle drifts only horizontally. The accuracy of this method is limited by the ability of the experimentalist to resolve the change in the direction of drift with a change in a balancing voltage.

The second method is to record the voltage from the position of the particle as the charges are removed. The position of the particle is fixed with respect to the cross wires. This method was found to be less accurate. The particle position is adjusted by manipulating the AC and DC fields in such a manner that it "touches" the x and y cross wires. The balancing voltage is recorded ( $V_1$ ). After irradiating with UV light the particle drifts to a new position. By adjusting the DC voltage ( $V_2$ ) the particle is brought back to it's former position. A series of measurements are made to evaluate  $\Delta V$ .

### 3.2.3 Particle Sizing

Illumination was provided by Spectra Physics Model 102-3 HeNe laser. The laser was mounted on a single axis translational stage and attached to a lead brick. This mounting coupled with a beam steerer allowed the laser beam to be directed into the chamber along the asymptote between the electrodes. The particles were observed and sized through a flat glass window at  $23^\circ$  to the illuminating beam using a Beck telescope with an image distance of 200 mm, a 50 mm objective, and a 10X Beck micrometer eyepiece. Sizing was accomplished by sweeping the movable reticle across the particle image. Adjusting the AC field to align one edge of the particle with the stationary stadia line gives the best results. This optical system allowed a resolution of 2.5  $\mu\text{m}$  in sizing particles. The UV light for electron stepping was provided by an Oriel 6035 low pressure mercury calibration lamp. The lamp was mounted in one of the ten chamber access ports.

### 3.3 RADIATION THEORY AND TWO-COLOR PYROMETRY

The task of obtaining time temperature profiles of singly burning graphite particle is not a simple one. Temperature might be low, the total duration of the burnout may be a few milliseconds, and particle sizes are on the order of microns. The nature of this project precluded the use of any nonoptical means for measuring surface temperature.

The light intensity of a burning graphite particle at any wavelength is proportional to the particle's surface area and a

strong function of temperature and emissivity. The radiant intensity is given by Planck's law (Fig. 6).<sup>15</sup>

$$E_{\lambda} = \frac{2\pi hc^2 e_{\lambda}}{\lambda^5} \left( \exp \left[ \frac{hc}{\lambda KT} \right] - 1 \right)^{-1} . \quad (7)$$

where  $c$  is speed of light,  $h$  is Planck's constant,  $K$  is Boltzmann's constant,  $T$  is particle temperature,  $\lambda$  is the wavelength and  $e_{\lambda}$  is the emissivity at that wavelength. The emissivity is a function of temperature.  $2\pi hc^2$  is Planck's first radiation constant,  $C_1$ , and equals  $3.74 \times 10^{-12}$  W cm<sup>-2</sup>. Similarly,  $hc/K$  is Planck's second radiation constant,  $C_2$ , and equals 1.44 cm °K. For  $\exp C_2/\lambda T \gg 1$ , i.e. for a maximum wavelength of observation of 900 nm and temperature below 3500° K, we can use Wein's approximation and disregard the unity term on the right hand side of Eq. (7). The radiative flux at  $\lambda$  is now given by

$$E_{\lambda} = \frac{e_{\lambda} C_1}{\lambda^5} \exp \left[ \frac{-C_2}{\lambda T} \right] . \quad (8)$$

Particle temperature cannot be directly determined using Eq. (8). The emissivity is unknown. In two-color pyrometry one is concerned not with absolute intensity at one wavelength but rather with the ratio of two intensities from two different wavelengths  $\lambda_A$  and  $\lambda_B$ . Assuming that emissivity is not a function of wavelength (grey body), the ratio  $e_A/e_B$  becomes unity and does not appear in the ratio of the emitted power at two different wavelengths,

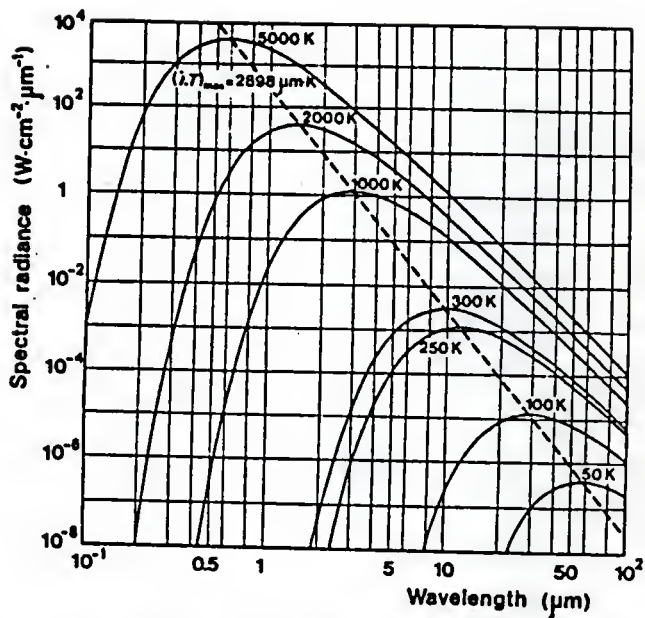


Fig. 6 The Planck distribution law; spectral radiance of blackbody radiation as a function of temperature and wavelength.

$$R(T, \lambda) = \frac{\int_{\lambda_{A-\lambda_1}}^{\lambda_{A+\lambda_1}} E_{\lambda A} d\lambda}{\int_{\lambda_{B-\lambda_1}}^{\lambda_{B+\lambda_1}} E_{\lambda B} d\lambda} . \quad (9)$$

The measured intensity at each wavelength will depend on system parameters such as the amount of light carried to the detectors and the detector efficiency. The latter is often dependent on wavelength. If the bandwidths are narrow, we can assume the average efficiency of the detectors within a bandwidth to be that of the peak wavelength. Equation (9) can be approximated as

$$R = \frac{I_A}{I_B} = \frac{\eta_{L,A} \eta_{D,A} \lambda_B^5 \Delta\lambda_A}{\eta_{L,B} \eta_{D,B} \lambda_A^5 \Delta\lambda_B} \exp \left( \frac{C_2}{T} \left( \frac{1}{\lambda_B} - \frac{1}{\lambda_A} \right) \right) . \quad (10)$$

where  $I_i$  are the measured intensities,  $\Delta\lambda_i$  are the bandwidths used in detection,  $\eta_{L,A}$  are the efficiencies for carrying light to the detectors and  $\eta_{D,A}$  are the detector efficiencies at each wavelength. All of the coefficients for the exponential term in the above equation can be combined into one calibration constant leaving

$$R = C \exp \left( \frac{C_2}{T} \left( \frac{1}{\lambda_A} - \frac{1}{\lambda_B} \right) \right) . \quad (11)$$

Equation (11) is graphed in Fig. 7. Inverting Eq. (11) one finds

$$T = \frac{C_2 \left( \frac{1}{\lambda_A} - \frac{1}{\lambda_B} \right)}{\ln R - \ln C} . \quad (12)$$

This approximation is valid for narrow bandwidths only.

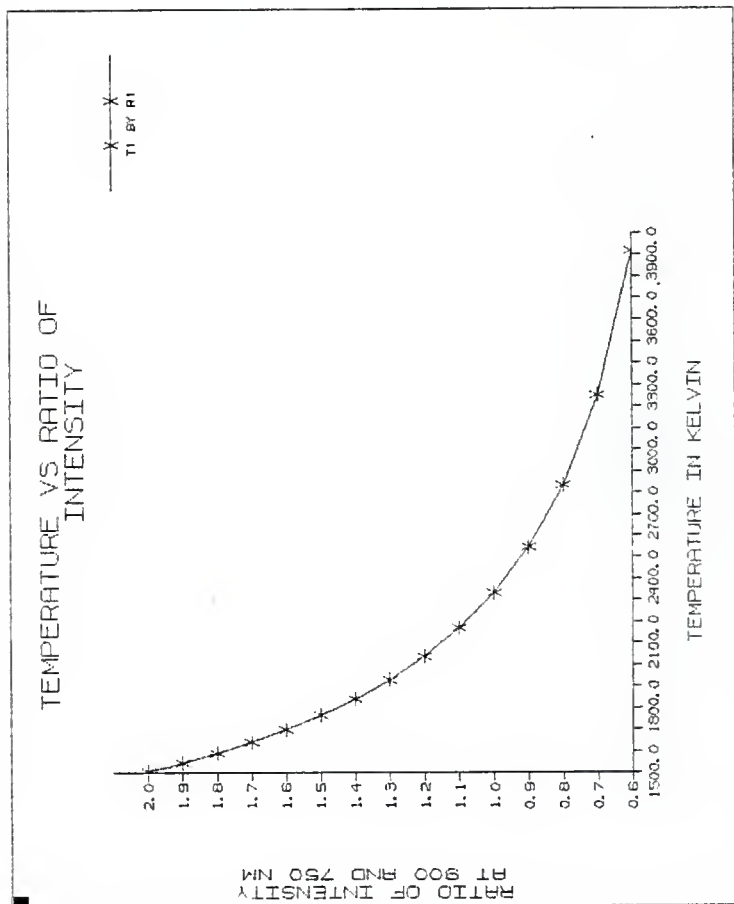


FIG. 7

### 3.3.1 Effect of Bandwidth on Ratio of Intensities

The bandwidth of the filters used was approximately 100 nm. This enabled us to obtain a larger signal and hence measure lower temperatures. Detailed calculations (Sec. 3.3.2) were made to see the effect of different bandwidths on the ratio of the intensities at two chosen wavelengths. Rather than using a point to point ratio, integrated "bands" beneath the radiation curve must be used. Corrections were made for filter transmission (part of  $\eta_L$ ) and detector efficiency ( $\eta_D$ ) so Eq. (9) is

$$R = C \frac{\int_{\lambda_A - \Delta\lambda_A/2}^{\lambda_A + \Delta\lambda_A/2} \eta_{L,A}(\lambda) \eta_{D,A}(\lambda) \lambda_A^{-5} \exp\left(\frac{-C_2}{\lambda_{AT}}\right) \Delta\lambda_A}{\int_{\lambda_B - \Delta\lambda_B/2}^{\lambda_B + \Delta\lambda_B/2} \eta_{L,B}(\lambda) \eta_{D,B}(\lambda) \lambda_B^{-5} \exp\left(\frac{-C_2}{\lambda_{BT}}\right) \Delta\lambda_B} \quad (13)$$

The functionalities of  $\eta_{Li}$  and  $\eta_{Di}$  have to be determined. If the bandwidths become too wide and being to overlap one another, the sensitivity of  $I_A/I_B$  to temperature diminishes. The calibration constant (C) now arises from the geometry of the system.

### 3.3.2 Effect of Bandwidth on Temperature Measurement

From Eq. (11) it is evident that the ratio of the two intensities  $I_A$  and  $I_B$  gives the temperature of the particle. Using Planck's law the ratio of intensities at the two wavelengths, namely, 900 and 750 nm were calculated for different temperatures as a function of the filter bandwidths. The results are listed in Table 1 and graphed in Fig. 8.

TABLE 1

WAVELENGTHS in nm		BANDWIDTH in nm	TEMPERATURE in K	RATIO $I_A/I_B$
900	750	10	2000	1.851
			2500	1.384
			3000	1.142
900	750	40	2000	1.850
			2500	1.385
			3000	1.143
900	750	80	2000	1.856
			2500	1.385
			3000	1.144
900	750	120	2000	1.838
			2500	1.384
			3000	1.145
900	750	200	2000	1.815
			2500	1.383
			3000	1.149
900	750	400	2000	1.717
			2500	1.372
			3000	1.165

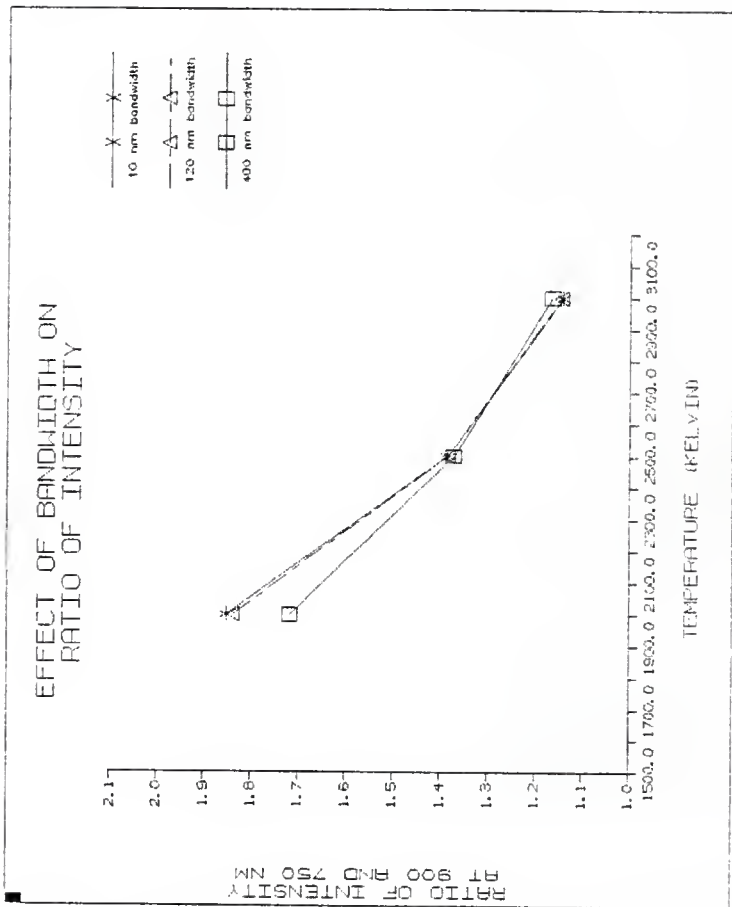


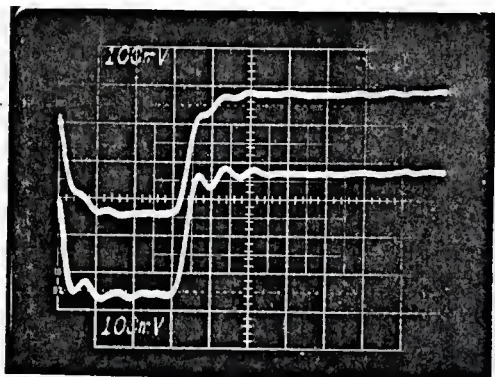
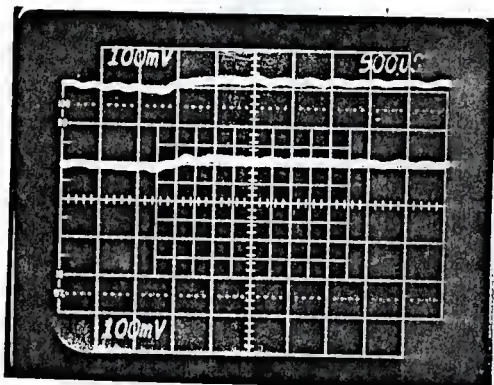
FIG. 8

FIGURE 9a

Intensity trace for a light bulb using a 10 nm filter. The experimental set-up consisted of a "chopper" in between an AC light bulb and the pyrometer. The "pulse" seen in the figure is approximately 300  $\mu$ s wide in the duration for which the pyrometer could "see" the light bulb.

FIGURE 9b

Intensity trace for a light bulb using a 100 nm filter. Time scale 500  $\mu$ s/division.

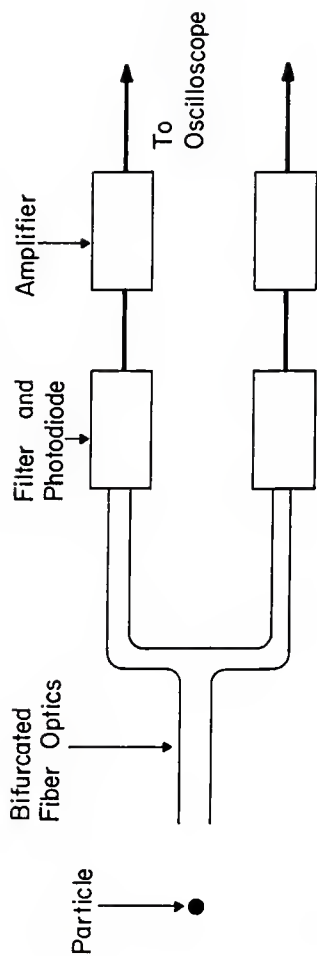


The analysis shows that the ratio of the intensities at the two wavelengths does not change significantly even if the bandwidth of the filters is varied from 10 to 100 nm, indicating that the temperature as measured from the ratios would be the same, but on the other hand the signal detected with a 100 nm filter would be 10 times that of a 10 nm bandwidth filter (Figs. 9a and 9b). Hence the signal to noise is greatly improved by using a 100 nm bandwidth filter without sacrificing the ratio, thereby giving a better accuracy in measuring the temperature.

#### 3.4 ACCESS TO BURNING PARTICLE

A three foot bifurcated fiber optic cable manufactured by Ealing was used to transmit the light signal from the particle to the pyrometer. A schematic of this set up is shown in Fig. 10. The advantages of using the fiber optic cable are manifold; namely:

- i) Radiation from the burning particle is received only a short distance from the particle thereby eliminating the need for optical focussing inside the Millikan Cell.
- ii) Reduction in noise level of the pyrometer since the AC interference of the ring electrode is minimized.
- iii) Permitted the design of the filter detector assembly and the signal receiving end of the system as separate units. The resulting versatility of the pyrometer has proved to be very advantageous.



Pyrometer Schematic

Fig. 10

### 3.4.1 Particle Simulation

Here I would demonstrate the ability of our pyrometer to measure temperature of a "typical" particle. Consider a graphite particle of radius (r), burning at a temperature T. The total black body power emitted by the particle at wavelength  $\lambda$  in the interval  $d\lambda$  is given by the expression

$$p = \frac{2\pi hc^2 d\lambda}{\lambda^5 \left[ \exp\left(\frac{hc}{\lambda KT}\right) - 1 \right]} \quad (14)$$

This power is radiated in all directions by the particle, a fraction of which is incident upon the fiber optics. The power incident on the fiber is

$$P = T.P \times A \times S_o$$

where T.P is total power emitted by the particle

A is the surface area of the particle

$S_o$  is the solid angle the fiber subtends on the particle

Considering losses associated with the fiber, filters, photodiodes and so forth (Fig. 11) the voltage signal detected by the oscilloscope is

$$V = T.P \times A \times S_o \times L_1 \times L_2 \times L_3 \times S_e \times R_f$$

where P is power incident on fiber

$L_1$  is the loss due to bifurcated fiber (50%)

$L_2$  is the transmission loss in fiber (50%)

$L_3$  is the transmission loss in filter (50%)

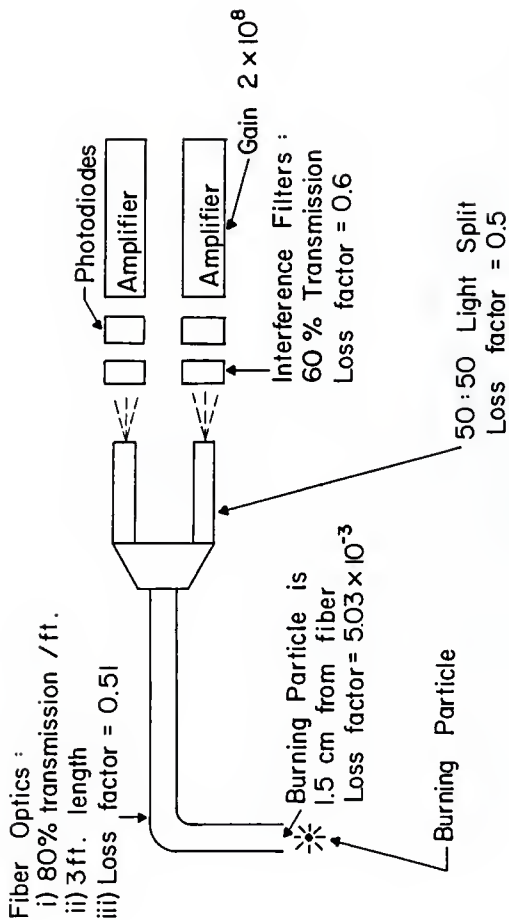


Fig.11 Analysis of Optical System

$S_e$  is the sensitivity of the photodiode (.3 A/W)

$R_f$  is the feedback resistor of the OPAMP (200 M $\Omega$ )

For a typical "particle" of radius 20  $\mu\text{m}$ , burning at a temperature of 1300° K, the total power emitted at 900 nm (100 nm interval) is 298.4 W/m<sup>2</sup>.

Surface area of the particle	5.026 x 10 <sup>-9</sup> m <sup>2</sup>
Solid angle subtended by fiber situated 1 cm from the particle	5.625 x 10 <sup>-3</sup>
Loss associated with bifurcation of fiber	0.50
Loss associated with fiber length	0.50
Transmission loss with filters	0.50
Sensitivity of photodiode at 900 nm	0.3 A/W
Feedback resistance of OPAMP	200 M $\Omega$

Substituting the above values in the previous equation gives a voltage signal of 60 mv. The noise level of the amplifier was 10 mv.

### 3.5 PYROMETER DESIGN

#### 3.5.1 Choice of Detectors

The temperature of the burning graphite particles was expected to be in the range of 1300 - 3000°K. A plot of the emitted energy vs wavelength for a black body source is given in Fig. 6. From the plot, in the temperature range of interest, the amount of radiant energy emitted at wavelengths below 700 nm is very small. In view

of this it was decided to use photodiodes rather than PMT's which have a better response in the infrared.

A second consideration in the choice of wavebands arises from the grey body assumption inherent in the determination of the temperature from the signal ratios for unknown  $e_{\lambda_A}$  and  $e_{\lambda_B}$ . The assumption that  $e_{\lambda_A} = e_{\lambda_B}$  is best for  $\lambda_A$  close to  $\lambda_B$ . A third consideration is that, for a good precision in determining T from R,  $dR/dT$  should be large.  $dR/dT$  is greatest in the visible and near infrared ( $\lambda_A$  close to  $\lambda_B$ ).

The chosen bands  $\lambda_A = 900$  nm,  $\lambda_B = 750$  nm and  $\Delta\lambda_A = \Delta\lambda_B = 100 \pm 20$  nm met all the requirements. Bandpass interference filters matching these specifications were obtained from Andover Corporation. The peak transmission of these filters is about 65-70%. The photodiodes chosen were S874-5K silicon photocells manufactured by Hamamtsu Corporation. The sensitivity is approximately 0.3 A/W at these two wavelengths and the active photosensitive area is 5.6 mm<sup>2</sup>.

### 3.5.2 Signal Processing

Two amplifiers with a gain of  $2 \times 10^8$  were built to amplify the detected signals. RCA SK9378 Bimos OPAMP were chosen for their fast response and low noise. The schematic of the current amplifier is shown in Fig. 12. Because of the small currents being measured ( $10^{-9}$  Amp), shielding considerations were important for the input signals and amplifiers.

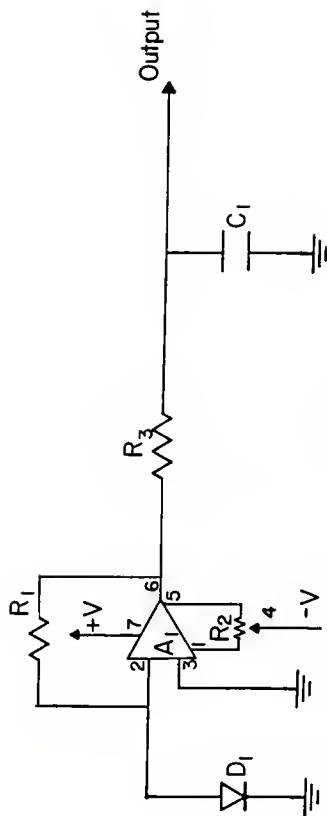


Fig.12 Current Amplifier Circuit

- A1 OPAMP SK 9378
- D1 Photodiode S874 - 5K
- R1 Resistor 200 M $\Omega$
- R2 Potentiometer 20 K $\Omega$
- R3 Resistor 1 K $\Omega$
- C1 Capacitor 0.1  $\mu$ F

### 3.5.3 Shielding Consideration

Even though the amplifier circuit looks quite simple (consisting of an OPAMP, resistor and capacitor), shielding considerations are vital in designing circuits dealing with low level currents.

Once the OPAMP (SK 9378) was chosen, the next step was to optimize circuit performance. Because the amplifiers extraordinary sensitivity makes high performance applications, error considerations which are insignificant in less sophisticated applications now become the limiting factor in circuit operation.

Hard wiring with good quality insulation (teflon) was preferred to printed circuit wiring. The amplifier was plugged into a socket with teflon insulators rather than soldered directly onto a printed circuit board. Insulated wires connected input terminals to external components. Further, all wiring was short and supported in such a way that movement due to vibration is limited as much as possible, because motion of input wiring will cause corresponding variations in parasitic capacitance.

Coaxial cable was used wherever possible to minimize RF pickup. Metal film resistors were chosen for their low noise, good temperature stability, low shunt capacitance and relatively low cost. Polystyrene capacitors were used for decreased leakage resistance. Finally, the amplifier and photodiodes were enclosed in an aluminum container to shield the 60 Hz.

### 3.6 Calibration of Pyrometer

Calculation of temperature information from the pyrometer outputs required determining the constant in Eq. (11). Calibration was performed using a Sylvania DXW 1000 W bulb operating at a standard temperature of  $3200 \pm 50^\circ\text{K}$ . Information about the quality of this lamp and its use as a source of spectral irradiation is provided by the Infrared Handbook.<sup>17</sup> For actual calibration runs with the DXW lamp, the pyrometer was shielded from stray light rays and the two base lines (900 & 750 nm) were made to coincide at a set line on the dual trace scope. The DXW lamp was placed at a fixed distance from the pyrometer and the response photographed on a polaroid film. To prevent reflected light from entering the pyrometer, the optical fiber was encased in a black casing. This proved effective since the ratio of intensities did not vary significantly even if the lamp was moved from the pyrometer. The calibration constant can be calculated from Eq. (12).

$$T = \frac{C_2 \left( \frac{1}{\lambda_B} - \frac{1}{\lambda_A} \right)}{\ln R - \ln C} .$$

Substituting the value of the known quantities viz.  $T = 3200^\circ\text{K}$ ,  $C_2 = 1.44 \text{ cm}^\circ\text{K}$ ,  $\lambda_A = 900 \text{ nm}$ ,  $\lambda_B = 750 \text{ nm}$  and the ratio of the intensities  $R$  calculated from the polaroid photograph, the constant  $C$  can be evaluated. The constant  $C$  varied by 8% in 10 days as a function of time and hence had to be determined before each run.

### 3.7 PYROMETER RESPONSE TIME

Figure 13 describes the schematic for determining the pyrometer response time. The mechanical chopper consisted of a circular disk driven by a motor. A small aperture (at a distance of 5.5 cm from the center of the disk) was made to allow "chopping" of the HeNe laser beam. The laser beam was focussed (convex lens) on the plane of the disk. The time period of revolution of the chopper was determined from the oscilloscope trace. One can find the linear velocity at the "aperture" using the simple relation,

$$V = \frac{2\pi R}{T} . \quad (15)$$

where  $V$  is the linear velocity at the "aperture".

$R$  is the distance between the "aperture" and center of the disk. (5.5 cm).

$T$  is the time period of revolution (24 ms).

Substituting the above values in Eq. (15) we get  $V$  as  $1.44 \times 10^3$  cm/sec. The beam radius of the laser at the focal point can be obtained from the relation

$$\omega_1 = \frac{\lambda f}{\omega_0 \pi} . \quad (16)$$

where  $\lambda$  is the wavelength of the laser beam (0.63  $\mu\text{m}$ ).

$f$  is the focal length of the lens (5.7 cm).

$\omega_0$  is the beam radius of the unfocussed beam (1 mm).

Hence the diameter of the focussed beam ( $2\omega_1$ ) is  $2.3 \times 10^{-3}$  cm.

$L_1$  - Convex Lens      F.O. - Fiber Optics

$C_1$  - Mechanical Chopper       $A_1, A_2$ -Detector and Amplifier assembly

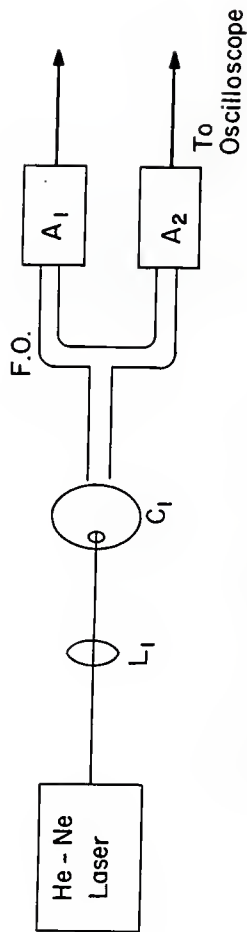


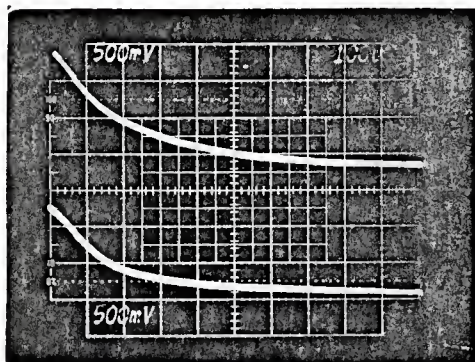
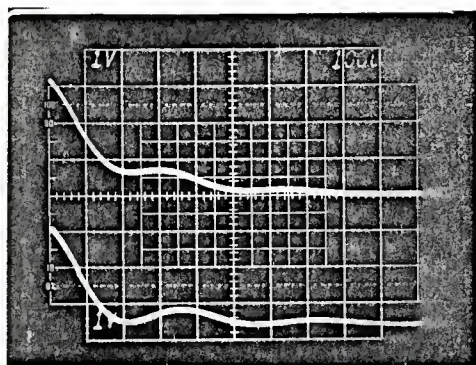
Fig. 13 Pyrometer Response

FIGURE 14a

Pyrometer output for response time.  
Time scale 100  $\mu$ s/div.  
Offset voltage of OPAMP 20 mV.

FIGURE 14b

Pyrometer output for response time.  
Time scale 100  $\mu$ s/div.  
Offset voltage of OPAMP 800 mV.



This gives a theoretical chopping time ( $2\omega_1/V$ ) of 15 us. The response time of the pyrometer as shown in Fig. (14b) is 200 us.

### 3.8 EXPERIMENTAL PROCEDURE

This section details the sequence of operation for data collection. At the beginning of each run, the calibration constant C was determined as described in Section 3.6. The following procedure was followed for each set of experimental conditions.

- i) A single graphite particle "trapped", sized and massed as described in Section 3.2.
- ii) By manipulating the DC field, the particle was made to pass through the Ar ion laser beam until a trace was obtained on the memory oscilloscope.
- iii) The particle was massed and the temperature was measured from the ratio of intensities.
- iv) Repeat conditions starting at (i) for a "fresh" particle or same particle if still present in the field of view.

#### 4. RESULTS AND DISCUSSION

A variety of information can be derived from the pyrometer outputs. The ratio of the outputs at two different wavelengths gives the temperature. A single pyrometer output depends upon the particle size and the ambient environment around it.

##### 4.1 PYROMETER OUTPUT FOR A LIGHT BULB

A standard 75 W light bulb operating at 110 v and 60 Hz was used to test the response of the pyrometer. The experimental set-up is similar to Fig. 10 except that the HeNe laser was replaced by the light bulb. The pyrometer output and the temperature profile are given in Fig. (15). The reader is encouraged to find the AC frequency from the pyrometer output.

##### 4.2 SINGLE PARTICLE TRACES

All of the raw data in this study was in the form of two traces on the screen of a memory oscilloscope (900 nm at the top and 750 nm at the bottom). Unless otherwise stated the time scale is 500us/div and voltage scale is 100mv/div on all the traces. Polaroid pictures of the traces used to find time-temperature histories are listed in the appendix.

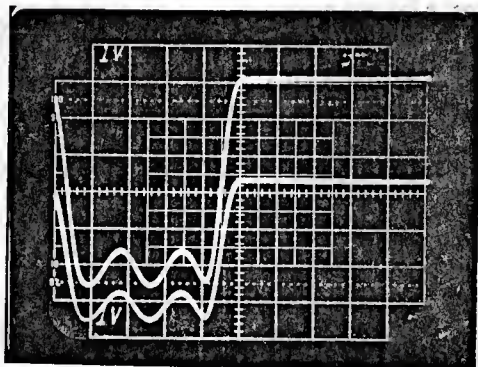
Figure (16) is a typical polaroid trace. The signals are inverted and appear here as they did on the oscilloscope. Time increases from left to right. The time-temperature analysis was computed as given in Table 2.

FIGURE 15a

Intensity trace of a 50W AC light bulb. The top and bottom traces are using 900 and 750 nm filters. Time scale 5 ms/div.

FIGURE 15b

Temperature profile for Fig. 15a.



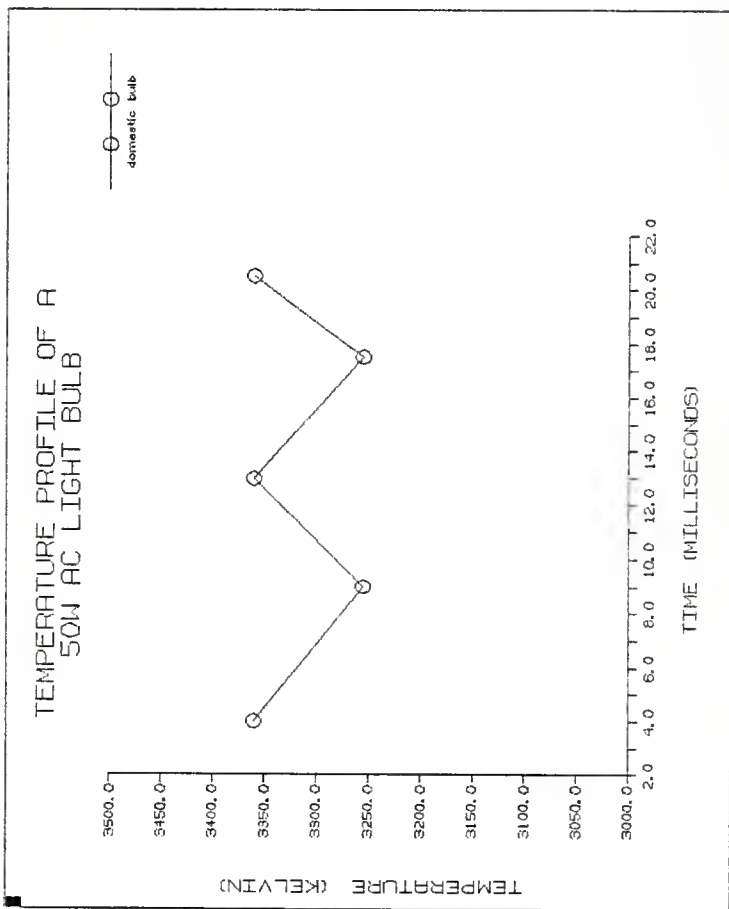


FIG. 15B

TABLE 2

Time in Microseconds	Ratio of Intensity at 900 and 750 nm (cm/cm)	Temperature in Kelvin
500	0.95/0.5	1593
700	1.9/1.1	1679
900	3.4/2.1	1743
1100	3.95/2.15	1622
1300	3.6/1.8	1550
1500	2.7/1.3	1519
1700	1.9/0.7	1335
1800	1.4/0.5	1317
1900	1.2/0.37	1235

The temperatures were calculated from the ratios using Eq. 12. The value of the calibration constant C was found by substituting the ratio of intensities at 900 and 750 nm obtained from the pyrometer response to the 1000W DXW bulb operating at  $3200 \pm 50^\circ\text{K}$ . The ratio in this case was 0.75 thereby giving a value of  $\ln(C) = 1.208$ . Temperature data for points from 0 to 500 us were not computed due to very low signals at 750nm (few millivolts). An error of 0.1cm in determining the height ( $I_B$ ) in this region could result in an error of  $200^\circ\text{K}$  in the temperature (Fig. 7).

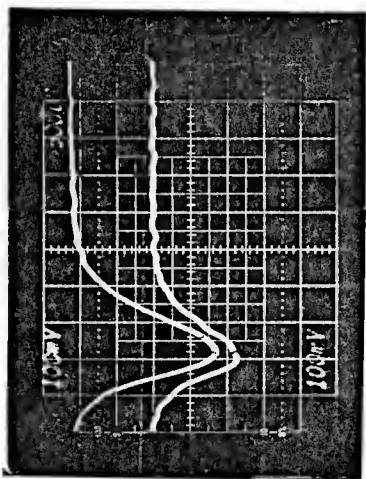
Oscillating intensities can be seen in Fig. 17. There exist at least four possible explanations for the oscillations:

- i) temperature is fluctuating
- ii) the particle rotates exposing different surface areas to the detector
- iii) the particle is moving in and out of the field of view
- iv) "ringing" in the amplifiers.

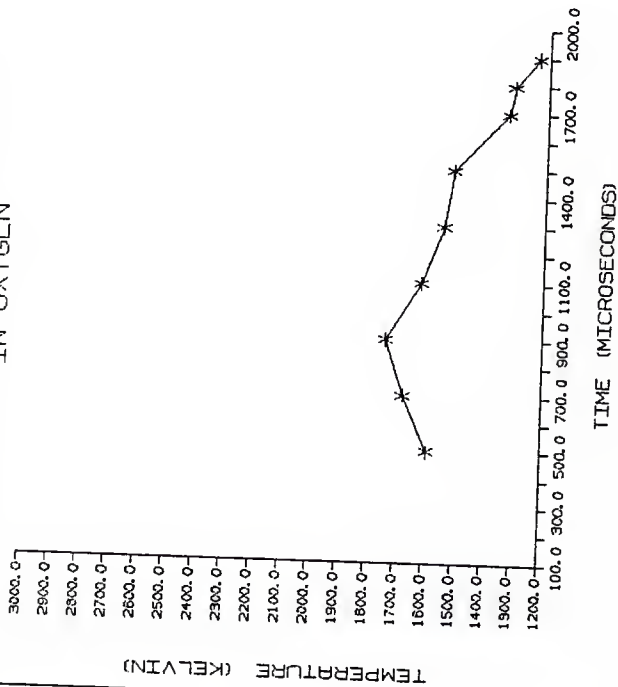
FIGURE 16a

Pyrometer output for a 30 $\mu$ m graphite  
particle heated by a laser.

Laser Power 0.32 W  
Ambient environment OXYGEN



TEMPERATURE PROFILE OF A  
GRAPHITE PARTICLE BURNING  
IN OXYGEN



X X  
128 BY TE28

FIG. 16B

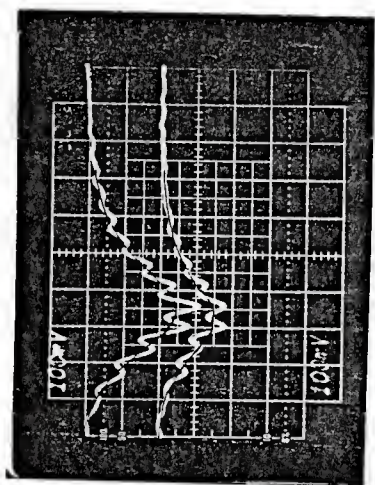


FIG. 17

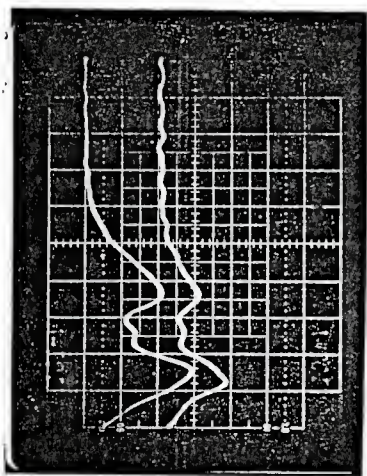


FIG. 18

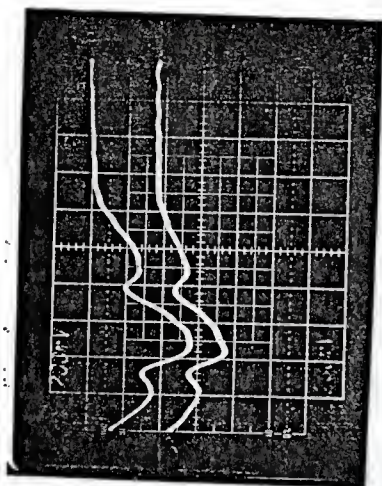


FIG. 19A

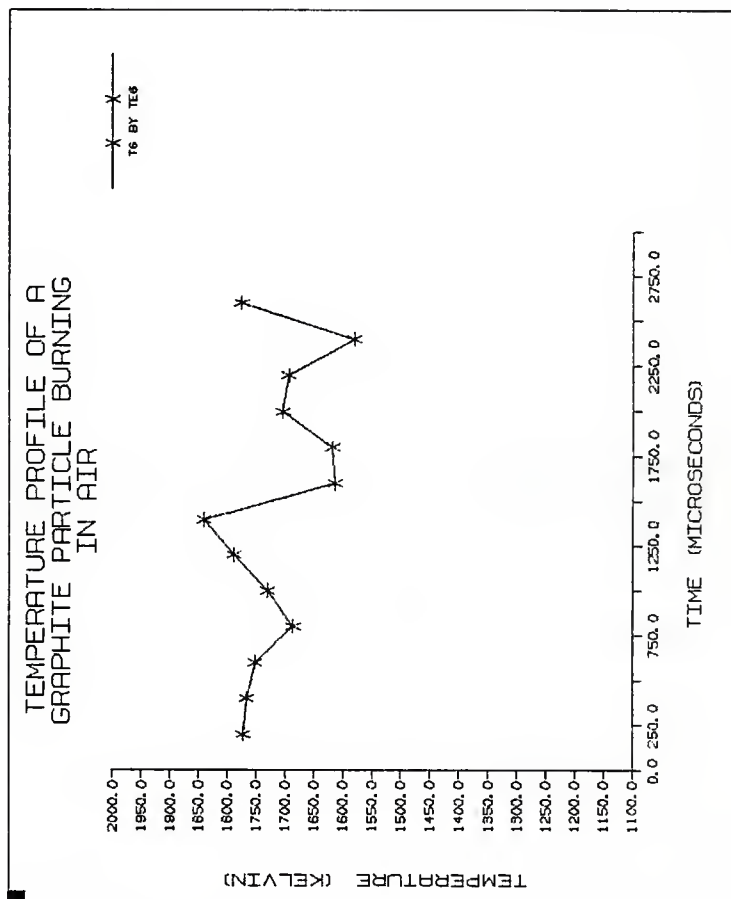


FIG. 19B

The profiles from several traces were analyzed to see if (i) was true. No exact correlation was seen between absolute intensity and temperature even though temperature did fluctuate. For traces showing oscillations and a definite rise/fall behavior in absolute intensity, a curve was drawn through the middle of each trace. Measurements were made using this curve (Fig. 17). The error introduced by this method was quite large. Figure 18 is included to give an example of a "suspicious" trace. It is quite possible that a second particle (obtained due to fragmentation of the "parent" particle) ignited before the first had extinguished, and the traces from both appear as one on the oscilloscope. This explanation was confirmed in some cases by visual observations. Possibility (iii) was ruled out since the diameter of the optical fiber was 3mm (3000um) and the particle oscillations were confined to 800um only. The author investigated (iv) further since it was the prime "suspect". The pyrometer response-time experiment was performed, with the time scale at 100us/div. The inquisitive reader might notice (Fig. 14a) "fine" oscillations occurring at an interval of about 300 us or 3 KHz. This was the "ringing" frequency found in most of the traces showing oscillatory behavior. Efforts to smoothen these oscillations by changing the offset voltage of the OPAMP's to several hundred millivolts were futile.

In most cases 10 or more data points were determined for each trace. Sufficient data was collected to justify the smooth curve approximation, but the main reason for providing the time-temperature graphs is to illustrate how temperature can vary

within a single trace. For a majority of the traces there appears to be a rise-fall behavior in temperature as well as absolute intensity though there are traces where temperature rises as the absolute intensity falls. Figures 19a and 19b illustrate this point and this might well be an experimental "artifact". In all the time-temperature graphs, the data points are connected by a straight line. This could be somewhat inappropriate and misleading, but is the clearest and best representation of the data available.

#### 4.3 MEAN PARTICLE BEHAVIOR

Several runs were made to test the effects of ambient environment (oxygen, nitrogen and air) and particle size. A summary of the data is presented in Table 3 and Figures 20 through 28.

TABLE 3

Ambient environment AIR  
 Laser power 0.30W  
 Laser beam diameter 22 um

Particle Size in Microns	Peak Temperature in Kelvin	Particle Heating time in us (FWHM)
20	2137	1100
22	1772	1400
22	2187	900
27	1752	3500
27	2573	800
33	1868	600

Ambient environment    NITROGEN  
 Laser power            0.30-0.32W  
 Laser beam diameter    22 um

Particle Size in Microns	Peak Temperature in Kelvin	Particle Heating time in us (FWHM)
25	1738	1300
25	1740	1000
Above particle heated again	1679	2100
27	1847	500
27	1758	1200
30	1427	900
Above particle heated again	1629	900
30	1654	1200
Above particle heated again	1834	1200

Ambient environment    OXYGEN  
 Laser power            0.34W/0.322\*  
 Laser beam diameter    22 um.

Particle Size in Microns	Peak Temperature in Kelvin	Particle Heating time in us (FWHM)
15	2059	1200
27	1883	2100
27	2648	400

Particle Size in Microns	Peak Temperature in Kelvin	Particle Heating time in us (FWHM)
30	1624	>2800
30	1762	1300
20*	2335	300
20*	2115	900
29*	2035	1300
Above particle heated again	1790	>2200
30*	1641	1300
Heated again	1743	1100
Heated again	1736	900
32*	1538	700
34*	1724	2000
Heated again	1842	>3500

Neglecting any of the smaller errors that may have arisen in the course of collecting and analyzing data, I would estimate an overall error in temperature of 50 to 150°K.

Despite the unusual behavior of the individual graphite, some consistent trends in average temperature profiles have been seen (Table 3 and Fig. 28). The most notable observation is that particles reach a higher peak temperature as diameter decreases and the particle heating time (FWHM) increases as the particle size increases. Particles ignited by the laser more than once achieved more or less the same temperatures thereby indicating that the

GRAPHITE PARTICLES BURNING  
IN AIR  
LASER BEAM DIAMETER 55UM

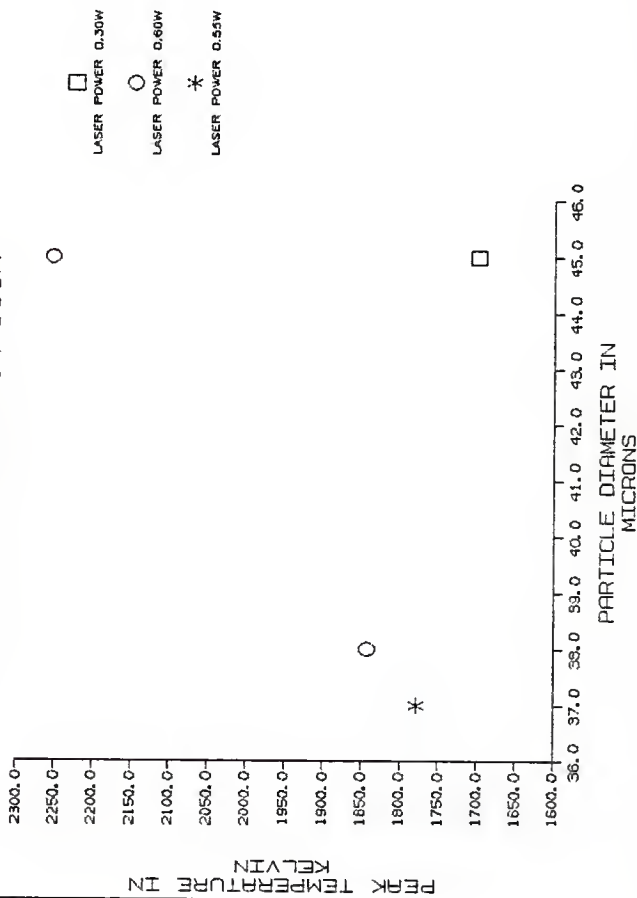


FIG. 20

GRAPHITE PARTICLES BURNING  
IN AIR  
LASER BEAM DIAMETER 55UM

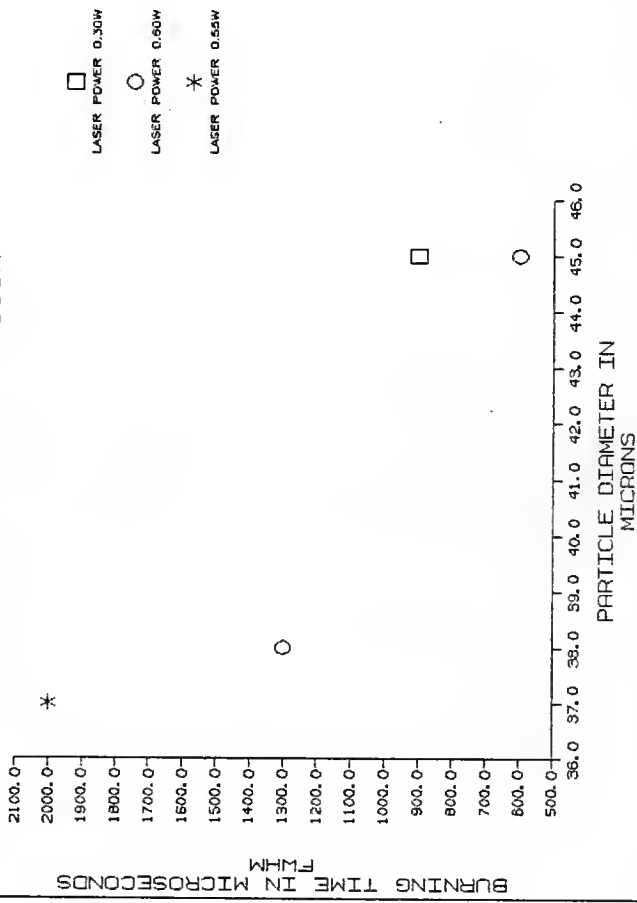


FIG. 21

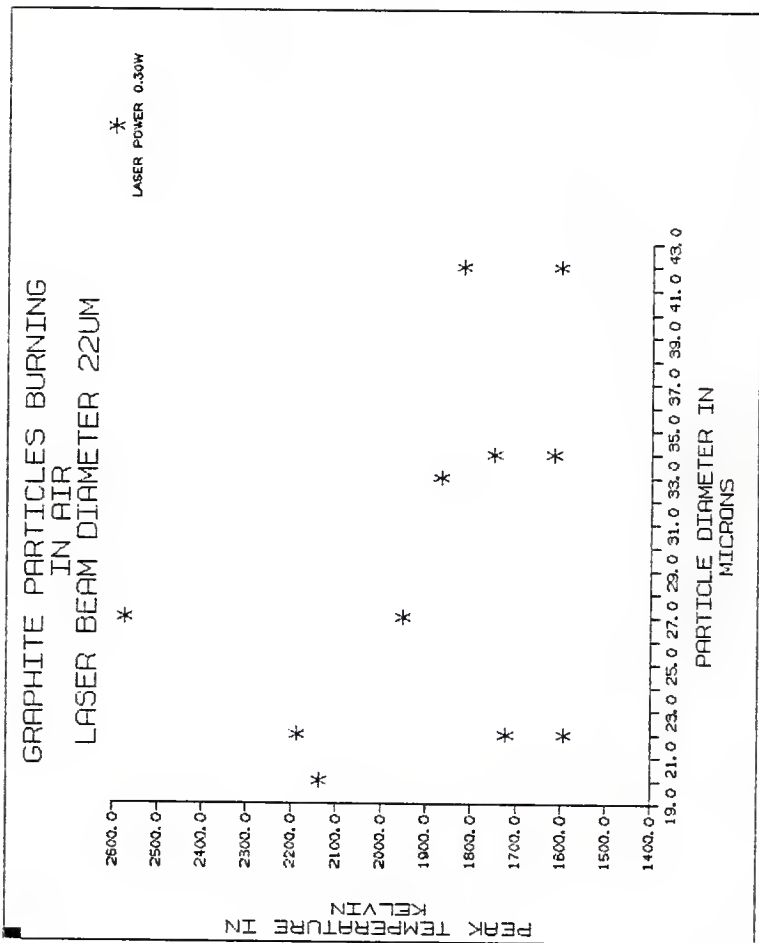


FIG. 22

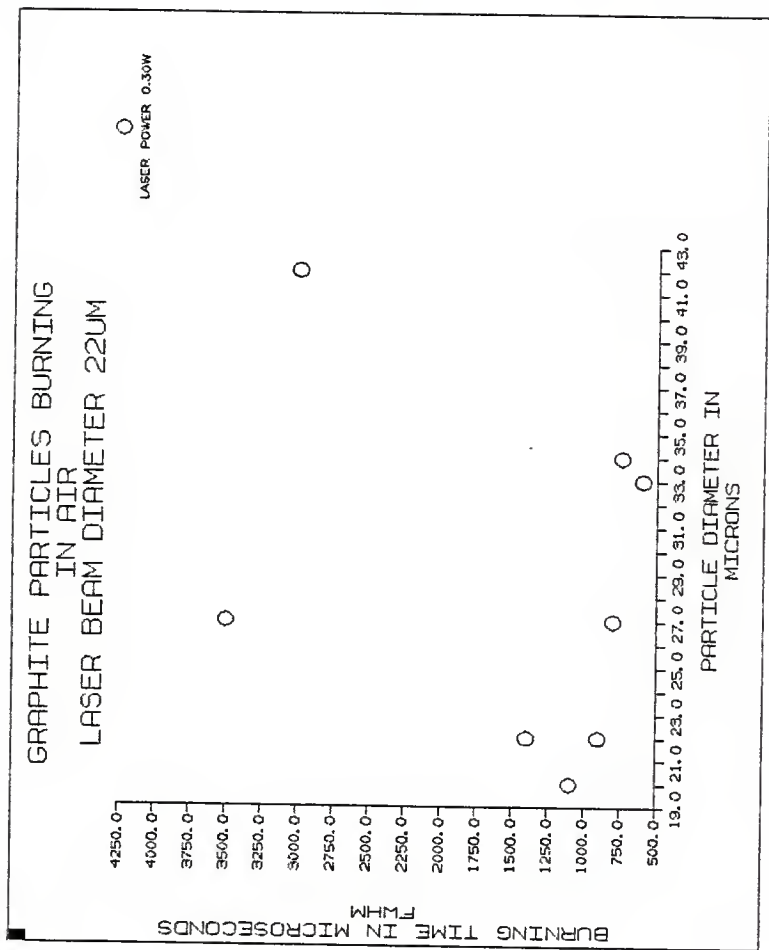


FIG. 23

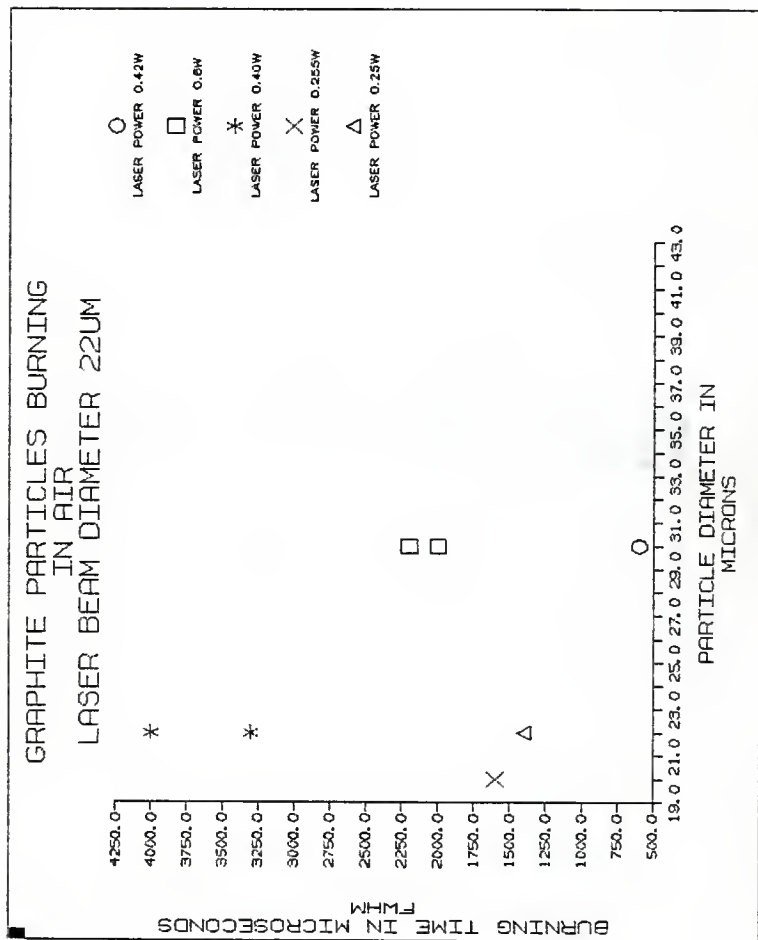


FIG. 24

GRAPHITE PARTICLES BURNING  
IN AIR  
LASER BEAM DIAMETER 22UM

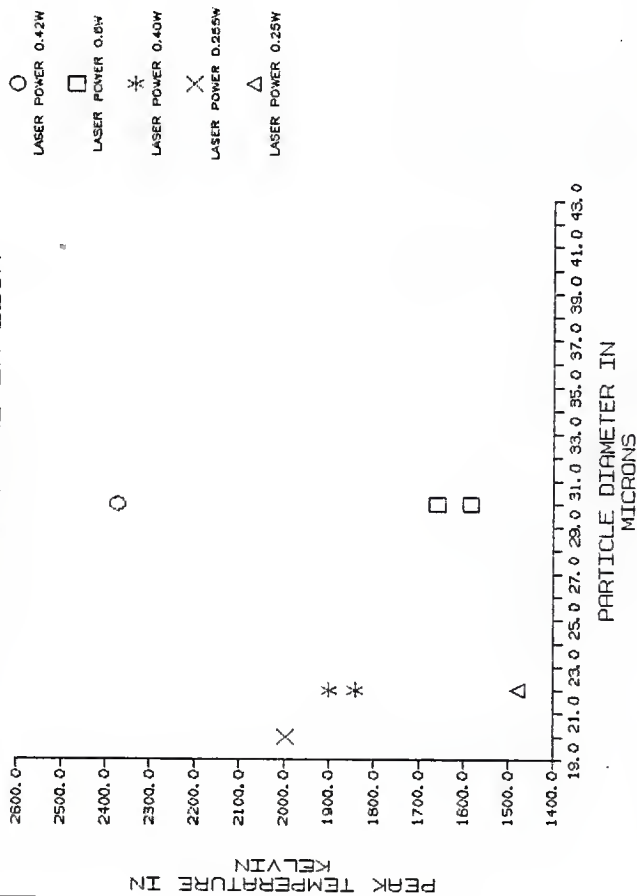


FIG. 25

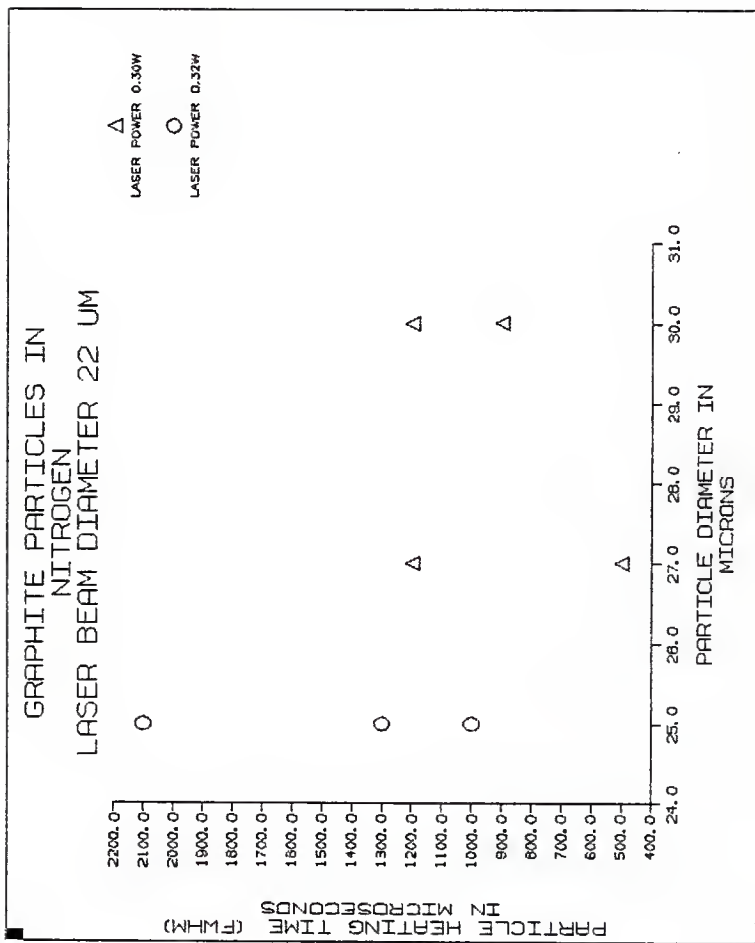


FIG. 26

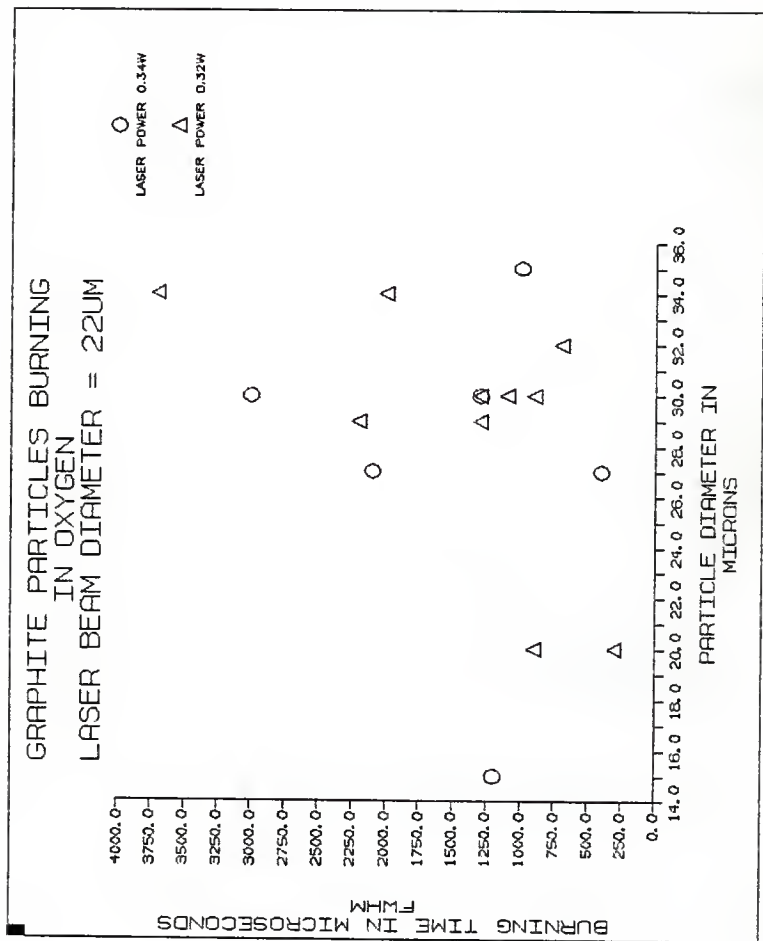


FIG. 27

GRAPHITE PARTICLES IN  
OXYGEN/NITROGEN  
LASER BEAM DIAMETER 22UM

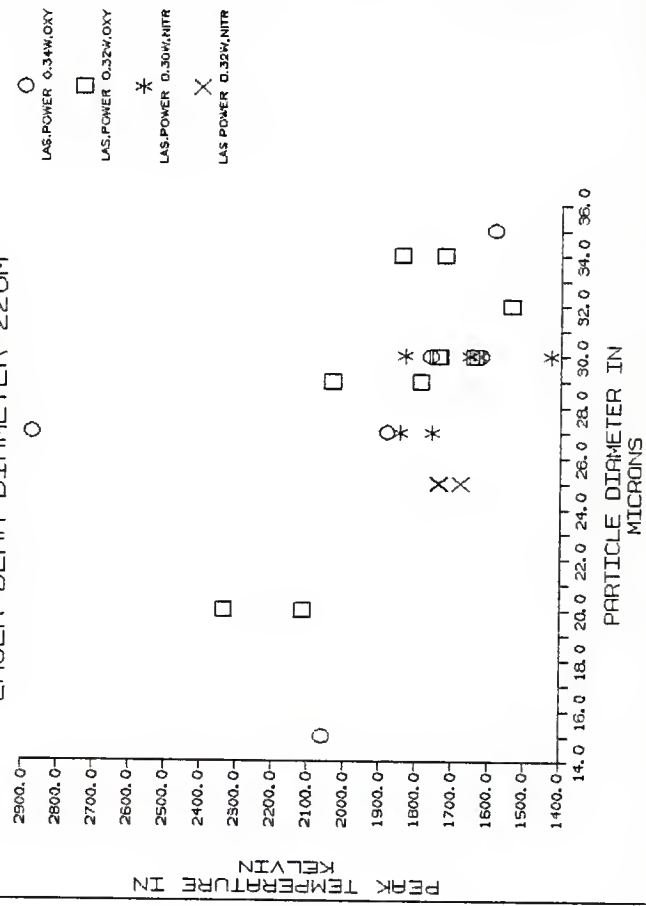


FIG. 28

particles did not burn. No significant temperature difference was noted for particles ignited in nitrogen and oxygen (Fig. 28). This leads the author to conclude that particles with diameters in the range 10-50  $\mu\text{m}$  could not sustain combustion and extinguished a few microseconds after the ignition pulse, if in fact they ignited at all. The laser power could be increased high enough to raise the particle temperature to nearly 2800°K. In spite of such high energy pulses, the particles extinguished without any significant burning.

#### 4.4 ERROR ANALYSIS

Consider the sources of uncertainty in the mass calculation.

$$m = K \bar{V}^2 / \Delta V_e,$$

Differentiating,

$$\delta m = \frac{\partial m}{\partial K} \delta K + \frac{\partial m}{\partial \bar{V}} \delta \bar{V} + \frac{\partial m}{\partial \Delta V} \delta \Delta V. \quad (17)$$

K is constant for all mass calculations since it contains only geometric and physical constants. Thus, while K could cause a systematic error, it does not introduce any uncertainty from measurement to measurement.

To get the V term, V is measured over a very small range (1-2) at large voltage (250 V). Therefore, the contribution to the uncertainty of measurement is at most around 1%. For example, in the worst case with a V = 250 and a voltage range of 2 volts,

$$\frac{\partial m}{\partial \bar{V}} \delta \bar{V} = (K/\Delta V_e) 2\bar{V} \delta \bar{V}. \quad (18)$$

The contribution to the uncertainty would be at most 2%. The major source of uncertainty is the determination of  $\Delta V_e$ . Typically, values of  $V_e$  range from 5 to 60 mv. Since the precision in determining  $V_g$  is  $\pm 0.003$  v, the effects of 3 mv uncertainty can be large.

If  $V_e = 60$  mv, uncertainty is 5%

If  $V_e = 10$  mv, uncertainty is 30%

The degree to which I can calculate  $\Delta V$  is the key to the accuracy of the measurement. I improved my certainty of  $\Delta V$  in two ways. First, I know the particle size to  $\pm 2.5$   $\mu\text{m}$ , and I know the density of the material. This gives me a rough estimate of the mass. The rough knowledge of the mass prevents gross error in the calculation.

The accuracy to which I can measure the temperature by two-color pyrometry is dependent on the degree of accuracy to which I can measure the ratio of the intensities.

Let the heights (at a particular instant of time with reference to the base line) of the two traces be  $h_1$  and  $h_2$  (900 and 750 nm respectively). Therefore the ratio of the intensities is

$$R = \frac{h_1}{h_2} \quad (19)$$

Differentiating Eq. (19) and using only absolute values we get

$$\frac{dR}{R} = \frac{dh_1}{h_1} + \frac{dh_2}{h_2} \quad (20)$$

The uncertainty in the measurements of the heights could be off by 0.1 division and the error in the temperature would depend on the individual heights as shown by Eq. (20). A graph of ratio versus temperature is given in Fig. 7.

## 5. RECOMMENDATION FOR FUTURE WORK

Joseph Cerv<sup>1</sup> reported a mass loss in the range of 40 - 90% as a result of laser ignition. The author was however unable to verify these results with the Millikan chamber for the following reasons:

- i) The particles (20 - 50  $\mu\text{m}$ ) typically have a mass of  $10^{-8}$  -  $10^{-9}$  gm. This results in a typical  $\Delta V$  in the range 10 - 30 mv at 200 V. From the various  $\Delta V$  obtained it is very difficult to "guess" the  $\Delta V$  for one electron. To illustrate this point consider the "true"  $\Delta V$  for one electron to be 10mv. If the experimental  $\Delta V$ 's were 10, 20 and 30 mv then one encounters little problem in choosing the correct  $\Delta V$ . Given typical uncertainties in  $\Delta V$ , however, the experimental  $\Delta V$ 's would typically be 7, 22 and 28 mv thereby making the task of "guessing" the  $\Delta V$  for a single electron very difficult.
- ii) The mass of smaller particles (10 $\mu\text{m}$ ) could be determined by electron stepping because  $\Delta V$  is now significantly larger than its uncertainty, but these particles usually did not produce a "good" trace for time-temperature measurements. This is because these particles are too small and hence not bright enough to be detected by the pyrometer.

Improvements can be made in the present two-color pyrometer. PMT's could replace the photodiode-amplifier combination. This would improve the gain as well as eliminate "ringing". The data collecting system could be automated through interfacing with a computer. The resolving power of the telescope should be improved.

High speed cinemicrography could be coupled to the telescope to get the details of the "burning" process.

SECTION 6

APPENDIX

## 6.1 NOTATION

c	Speed of light $3 \times 10^8$ m/s
C	Calibration constant of pyrometer
$C_1$	Planck's first radiation constant $3.74 \times 10^{-12}$ W cm <sup>-2</sup>
$C_2$	Planck's second radiation constant 1.44 cm <sup>2</sup> K
h	Planck's constant $6.624 \times 10^{-34}$ J/s
$E_i$	Intensity of radiation at wavelength i
$e_i$	Emissivity at wavelength i
$\eta_{D,i}$	Efficiency of detectors at wavelength i
$\eta_{L,i}$	Efficiency of light transport at wavelength i
$\lambda$	Wavelength
$\Delta\lambda$	Bandwidth
$\pi$	3.14159
$\mu\text{m}$	microns
k	Boltzman's constant

## 6.2 COMPUTER PROGRAM

Given a series of balancing voltages  $V_g$ , this program arranges the  $V_g$ 's top to bottom in an increasing order. It then picks up the lowest  $V_g$  (topmost number) and subtracts it from the rest of the numbers. This process is repeated until only one value of  $V_g$  is left. The reader then "chooses" the  $V_e$  from the various values generated by the program.

```
PROGRAM MILI
C  DECLARE VARIABLES
   INTEGER PASS,MIN,NUM,I,START,NEXT,DONE
   REAL K(100),TEMP
```

```

C   READ IN VECTOR
    READ(5,*) (K(I), I=1, NUM)
C   PRINT DATA
    WRITE(7, 100) NUM
100  FORMAT('NUMBE OF ELEMENTS=', I4)
    WRITE(7, 200)
200  FORMAT('UNSORTED VECTOR')
    DO 30, I=1, NUM
30   WRITE (7, *) K(I)
    DONE=NUM-1
C   REPEAT FOR NUM-1 PASSES
    DO 1, PASS=1, DONE
    MIN=PASS
    NEXT=PASS+1
    DO 2, I=NEXT, NUM
    IF(K(I).LT.K(MIN)) MIN=I
2   CONTINUE
    IF(MIN.NE.PASS) THEN
    TEMP=K(PASS)
    K(PASS)=K(MIN)
    K(MIN)=TEMP
    END IF
1   CONTINUE
C   PRINT SORTED VECTOR
    WRITE (7, 300)
300  FORMAT ('SORTED VECTOR')
    DO 40, I=1, NUM
40   WRITE(7, 500) K(I)
500  FORMAT(1X, FJ.3)
C   THIS DOES SOMETHING
    WRITE(7, 400)
400  FORMAT('EXTRA OUTPUT')
    DO 3, START=1, NUM-1
    DO 4, I=START+1, NUM
    K(I)=K(I)-K(START)
4   WRITE(7, 500) K(I)
3   CONTINUE
    STOP
    END

```

APPENDIX 6.3

Data sheet for pyrometer components

# STANDARD BANDPASS FILTERS

	CWL (NM)	FWHM (NM)	# OF CAV	FILTER TYPE		MINIMUM PEAK T %	N*	MAXIMUM THICKNESS (MM)	PART NUMBER	
				SEE PAGES	6-8				25mm OIA.	36mm DIA.
H	658.3 +2/-0	10±2	3	3	3	50	2.05	7.0	658FS10-25	658FS10-50
	660 +2/-0	10±2	3	3	3	50	2.05	7.0	660FS10-25	660FS10-50
	670 +3/-0	10±2	3	3	3	50	2.05	7.0	670FS10-25	670FS10-50
Li	670.8 +2/-0	10±2	3	3	3	50	2.05	7.0	671FS10-25	671FS10-50
	680 +3/-0	10±2	3	3	3	50	2.05	7.0	680FS10-25	680FS10-50
	690 +3/-0	10±2	3	3	3	50	2.05	7.0	690FS10-25	690FS10-50
Ruby laser	694.3 +2/-0	1±2	2	2	6	60	2.05	3.5	694FS01-25	694FS01-50
Ruby laser	694.3 +2/-0	1±2	2	2	2	40	2.05	8.5	694FS02-25	694FS02-50
Ruby laser	694.3 +3/-0	3±5	2	2	2	45	2.05	8.5	694FS03-25	694FS03-50
Ruby laser	694.3 +1.5/-0	10±2	3	3	3	50	2.05	7.0	694FS10-25	694FS10-50
	700 +3/-0	10±2	3	3	3	50	2.05	7.0	700FS10-25	700FS10-50
	706 +10/-0	40±8	3	3	3	45	2.05	7.0	706FS40-25	706FS40-50
	707 +25/-0	80±18	-	-	9	70	-	7.0	707FS80-25	707FS80-50
	710 +3/-0	10±2	3	3	3	50	2.05	7.0	710FS10-25	710FS10-50
	720 +3/-0	10±2	3	3	3	50	2.05	7.0	720FS10-25	720FS10-50
	730 +3/-0	10±2	3	3	3	50	2.05	7.0	730FS10-25	730FS10-50
	740 +3/-0	10±2	3	3	3	50	2.05	7.0	740FS10-25	740FS10-50
	750 +3/-0	10±2	3	3	3	50	2.05	7.0	750FS10-25	750FS10-50
	750 +10/-0	40±8	3	3	3	50	2.05	7.0	750FS40-25	750FS40-50
	750 +25/-0	100±20	-	-	9	70	-	7.0	750FS80-25	750FS80-50
	760 +3/-0	10±2	3	3	3	45	2.05	7.0	760FS10-25	760FS10-50
K	768.5 +2/-0	10±2	3	3	3	45	2.05	7.0	768FS10-25	768FS10-50
	770 +3/-0	10±2	3	3	3	45	2.05	7.0	770FS10-25	770FS10-50
Rb	780 +3/-0	10±2	3	3	3	45	2.05	7.0	780FS10-25	780FS10-50
	790 +3/-0	10±2	3	3	3	45	2.05	7.0	790FS10-25	790FS10-50
Rb	794.7 +2/-0	10±2	3	3	3	45	2.05	7.0	795FS10-25	795FS10-50
	800 +3/-0	10±2	3	3	3	45	2.05	7.0	800FS10-25	800FS10-50
	800 +10/-0	40±8	3	3	3	50	2.05	7.0	800FS40-25	800FS40-50
	800 +25/-0	100±20	-	-	9	70	-	7.0	800FS80-25	800FS80-50
	810 +3/-0	10±2	3	3	3	45	2.05	7.0	810FS10-25	810FS10-50
	820 +3/-0	10±2	3	3	3	45	2.05	7.0	820FS10-25	820FS10-50
GaAlAs laser	830 +3/-0	10±2	3	3	3	45	2.05	7.0	830FS10-25	830FS10-50
	840 +3/-0	10±2	3	3	3	45	2.05	7.0	840FS10-25	840FS10-50
	850 +3/-0	10±2	3	3	3	45	2.05	7.0	850FS10-25	850FS10-50
	850 +10/-0	40±8	3	3	3	50	1.45	7.0	850FS40-25	850FS40-50
	850 +25/-0	100±20	-	-	9	70	-	7.0	850FS80-25	850FS80-50
	860 +3/-0	10±2	3	3	3	45	2.05	7.0	860FS10-25	860FS10-50
	870 +3/-0	10±2	3	3	3	45	2.05	7.0	870FS10-25	870FS10-50
	880 +3/-0	10±2	3	3	3	45	2.05	7.0	880FS10-25	880FS10-50
	890 +3/-0	10±2	3	3	3	45	2.05	7.0	890FS10-25	890FS10-50
	900 +3/-0	10±2	3	3	3	45	2.05	7.0	900FS10-25	900FS10-50
	900 +10/-0	40±8	3	3	3	45	1.45	7.0	900FS40-25	900FS40-50
	900 +25/-0	100±20	-	-	9	65	-	7.0	900FS80-25	900FS80-50

FIGURE 29a

Transmission curve for the filter with peak wavelength 750 nm.

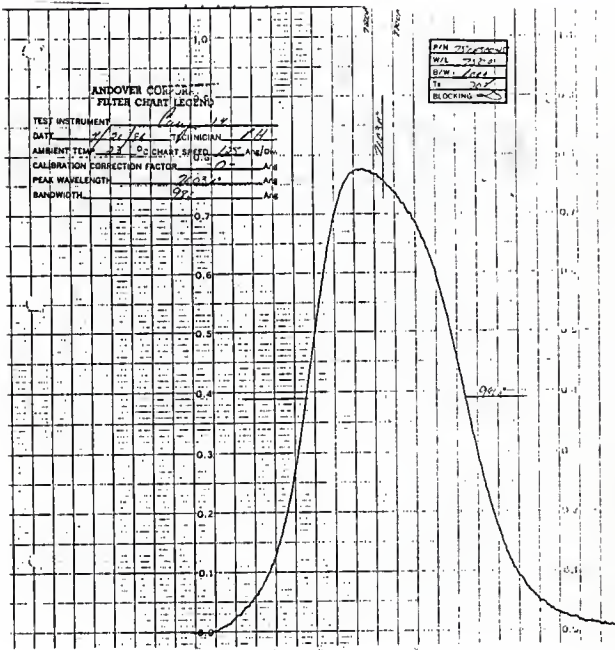
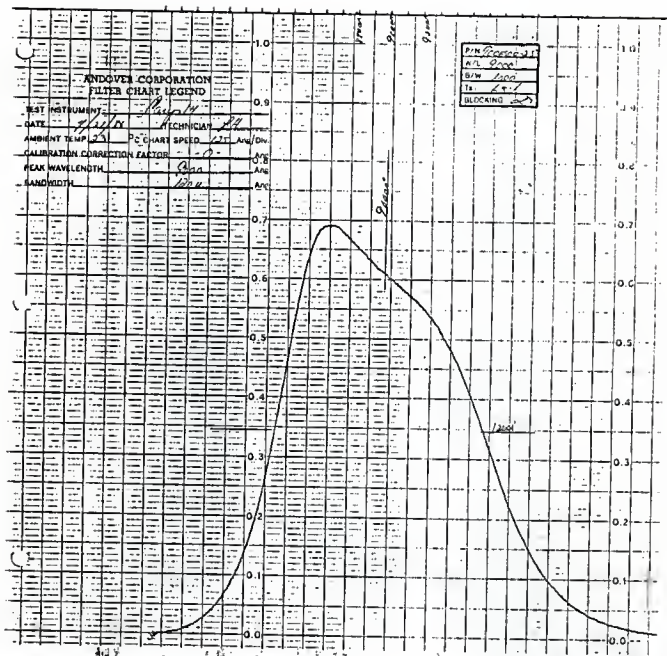


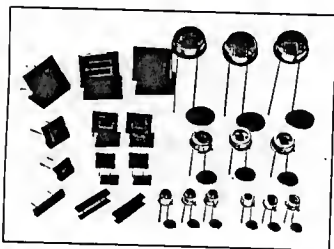
FIGURE 29b

Transmission curve for the filter  
with peak wavelength 900  $\mu\text{m}$ .



## S874, S875 Series (Visible to Near IR)

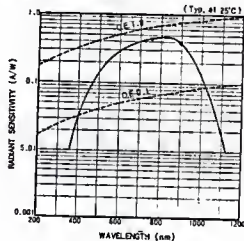
① Type No.	Outlines (P. 29, 30)	Photosensitive Surfaces		Package (mm)	Characteristics (@25°C)							
		Size (mm)	Effective Area (mm <sup>2</sup> )		Spectral Response		Typical Radiant Sensitivity (A/W)			NEP <sup>②</sup> Typ. (W/Hz <sup>1/2</sup> )	D* <sup>③</sup> Typ. (cm·Hz <sup>1/2</sup> /W)	
					Range (nm)	Peak Wavelength (nm)	Peak Wave- length	GaP LED (560nm)	He-Ne Laser (633nm)	GaAs LED (930nm)		
<b>S874 Series (Metallic Case)</b>												
S874-5K	④	2.5×2.4	5.6	TO-5	430-1060	850±50	0.45	0.2	0.3	0.3	8×10 <sup>-14</sup>	4×10 <sup>11</sup>
-5K	④	5.9×5.9	33	TO-8								
-18K	④	1.2×1.2	1.3	TO-18								
-18L	④											
<b>S875 Series (Ceramic Case)</b>												
S875-18R	④	1.1×5.9	5.8	2.7×15	430-1060	850±50	0.45	0.2	0.3	0.3	8×10 <sup>-14</sup>	4×10 <sup>11</sup>
-33R	④	2.5×2.4	5.6	8×7.5								
-66R	④	5.9×5.9	33	8.8×10								
-1010R	④	10.1×10.2	98	15×16.5								



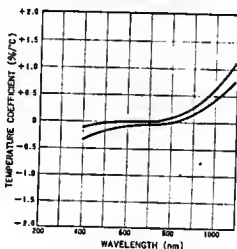
- ④ K: Borosilicate glass window
- R: Resin coating window
- L: Lens type borosilicate glass window
- ② NEP = Noise Current (A/Hz<sup>1/2</sup>)
- ③ Radiant Sensitivity at Peak (A/W)
- ④ D\* (D-star) =  $\frac{\text{Effective Sensitive Area (cm}^2\text{)}^{1/2}}{\text{NEP}}$

- ④ I<sub>ph</sub> = 10 (mA)
- ④ I<sub>ph</sub> = Dark Current at V<sub>rs</sub> = 10mV (A)
- ④ t<sub>r</sub> is the time required to transition from 10% to 90% of the normal high level output value. The light source is a GaAsP LED (655nm) and the load resistance is 1kΩ.

### • Spectral Response



### • Temperature Characteristic of I<sub>ph</sub>



## ● Spectral Response

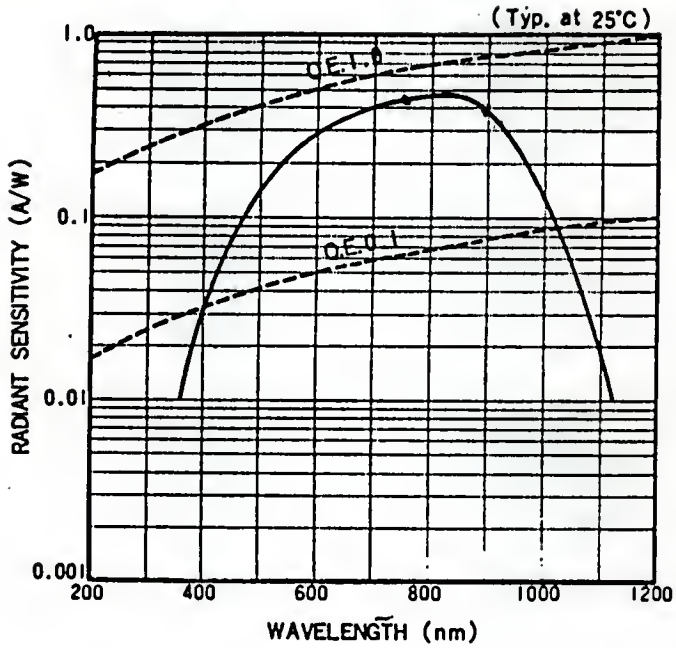


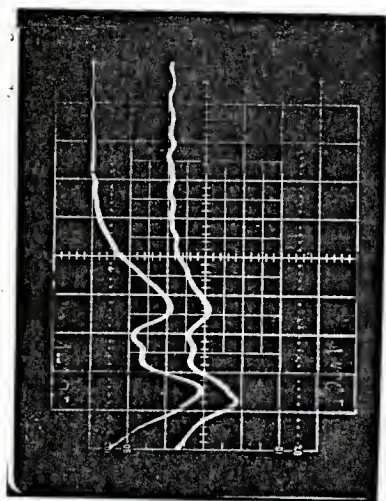
FIGURE 31a

Pyrometer output for a 45  $\mu\text{m}$  particle in air.

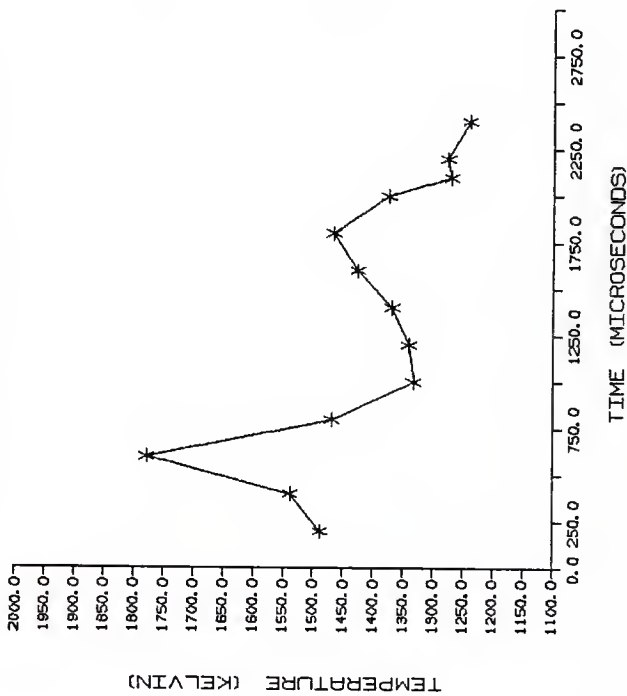
Laser Power	0.30W
Laser Beam Diameter	55 $\mu\text{m}$
Time Scale for this and the rest of the traces is	500 $\mu\text{s}/\text{div}$
Voltage Scale	100 $\text{mv}/\text{div}$

FIGURE 31b

Time-Temperature profile for the above.



TEMPERATURE PROFILE OF A  
GRAPHITE PARTICLE BURNING  
IN AIR



X X  
T1 BT TE1

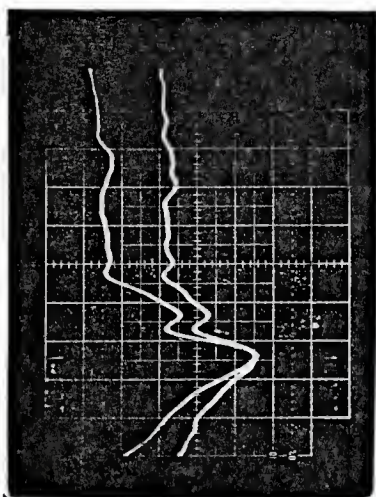
FIGURE 32a

Pyrometer output for a 42  $\mu\text{m}$  particle in air.

Laser Power	0.30W
Laser Beam Diameter	22 $\mu\text{m}$
Voltage Scale	100 mv/div.

FIGURE 32b

Time-temperature profile for Fig. (28a).



TEMPERATURE PROFILE OF A  
GRAPHITE PARTICLE BURNING  
IN AIR

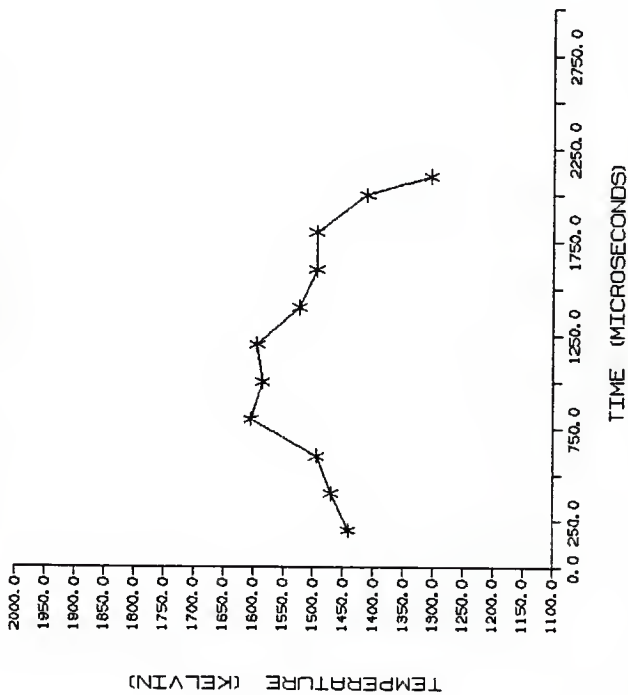


FIGURE 33a

Pyrometer output for a 30  $\mu\text{m}$  particle in air

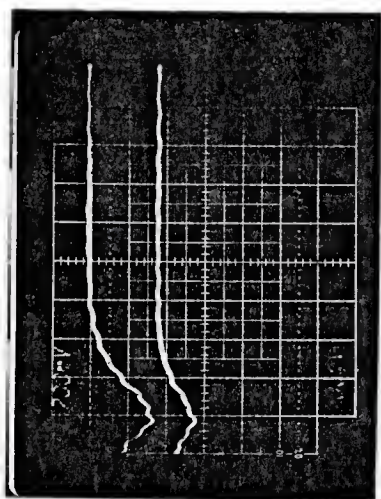
Laser Power 0.6W

Laser Beam Diameter for this and the remaining  
traces 22  $\mu\text{m}$

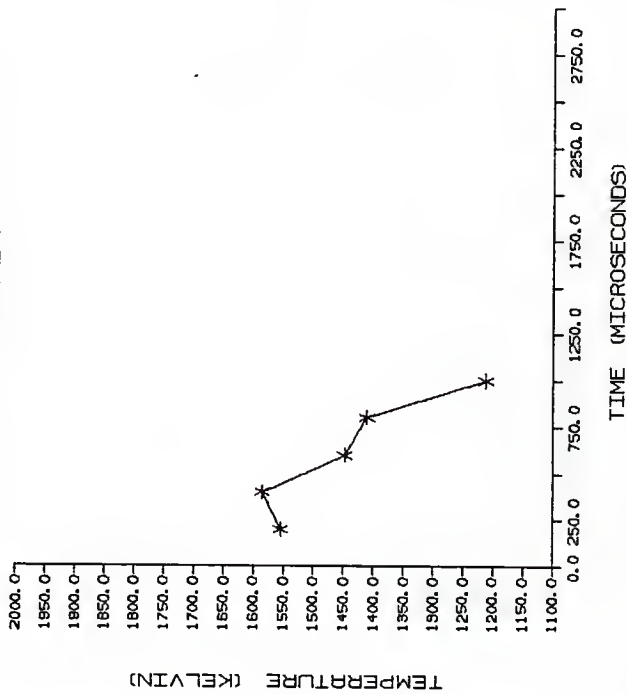
Voltage Scale 200 mv/div.

FIGURE 33b

Time-temperature profile for the above.



TEMPERATURE PROFILE OF A  
GRAPHITE PARTICLE BURNING  
IN AIR



X X  
T3 BY TES

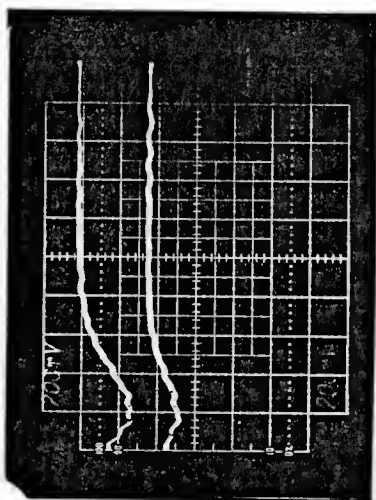
FIGURE 34a

Particle in figure 29a heated again

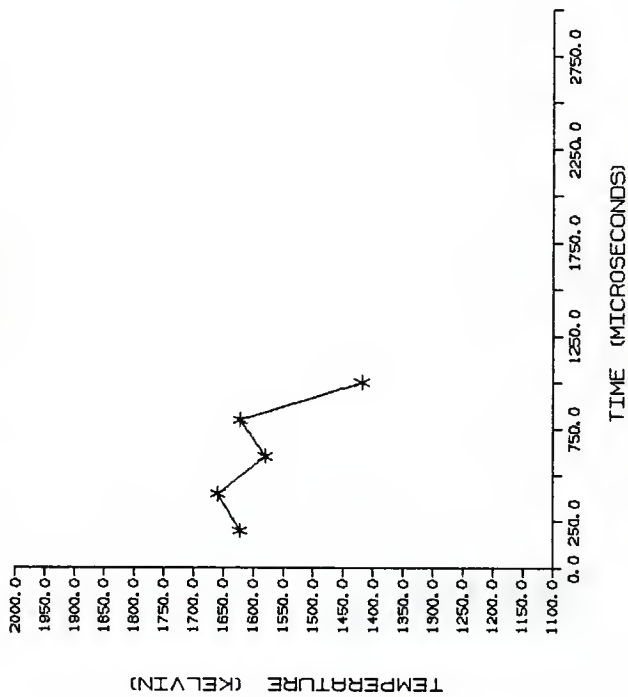
Laser Power 0.60W

FIGURE 34b

Time-temperature profile for the above.



TEMPERATURE PROFILE OF A  
GRAPHITE PARTICLE BURNING  
IN AIR



X — X  
T4 BY TE4

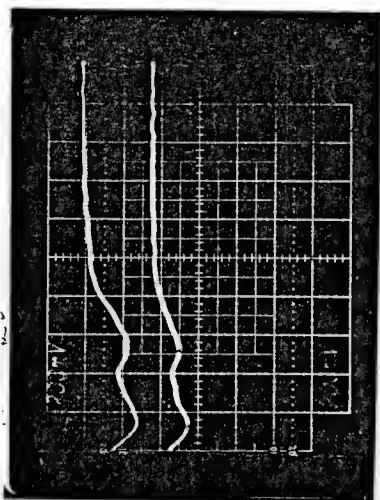
FIGURE 35a

Pyrometer output for a 22  $\mu\text{m}$  particle in air.

Laser Power	0.40W
Voltage Scale	200 mv/div.

FIGURE 35b

Time-temperature profile for the above.



TEMPERATURE PROFILE OF A  
GRAPHITE PARTICLE BURNING  
IN AIR

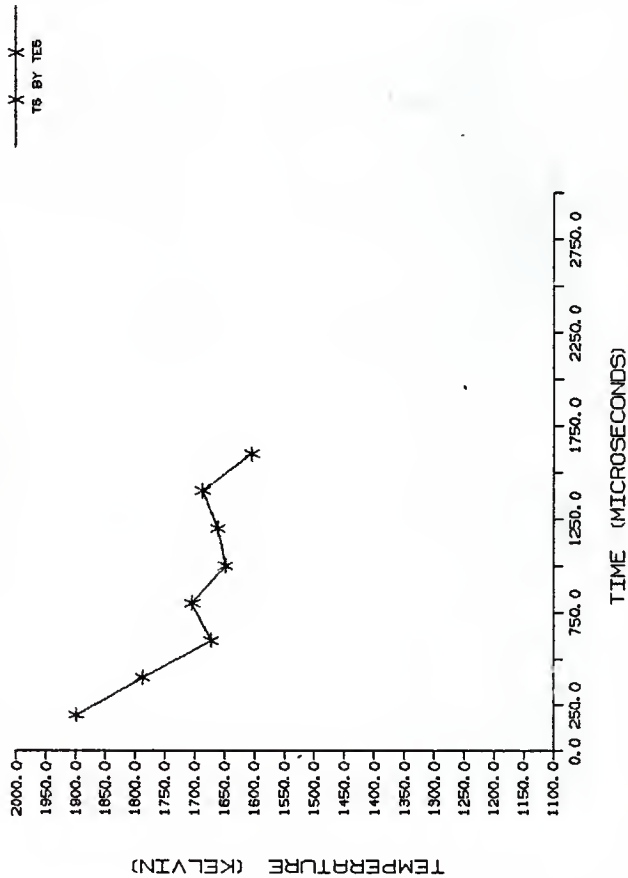


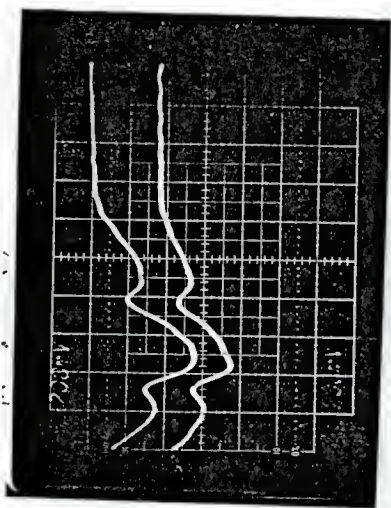
FIGURE 36a

Pyrometer output for the previous particle heated again

Voltage Scale            200 mv/div.

FIGURE 36b

Time-temperature profile for Fig. 36a.



TEMPERATURE PROFILE OF A  
GRAPHITE PARTICLE BURNING  
IN AIR

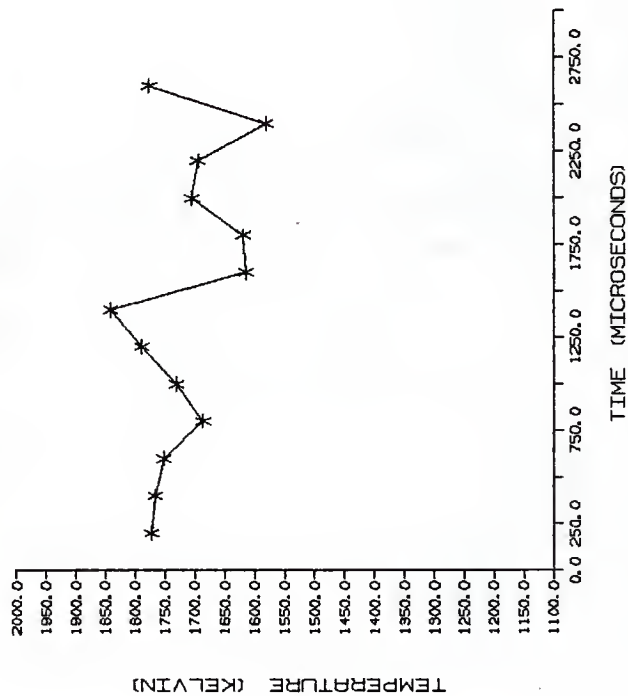


FIGURE 37a

Pyrometer output for a 22  $\mu\text{m}$  particle in air

Laser Power        0.30 W  
Voltage Scale      100 mv/div.

FIGURE 37b

Time-temperature profile for the above.



TEMPERATURE PROFILE OF A  
GRAPHITE PARTICLE BURNING  
IN AIR

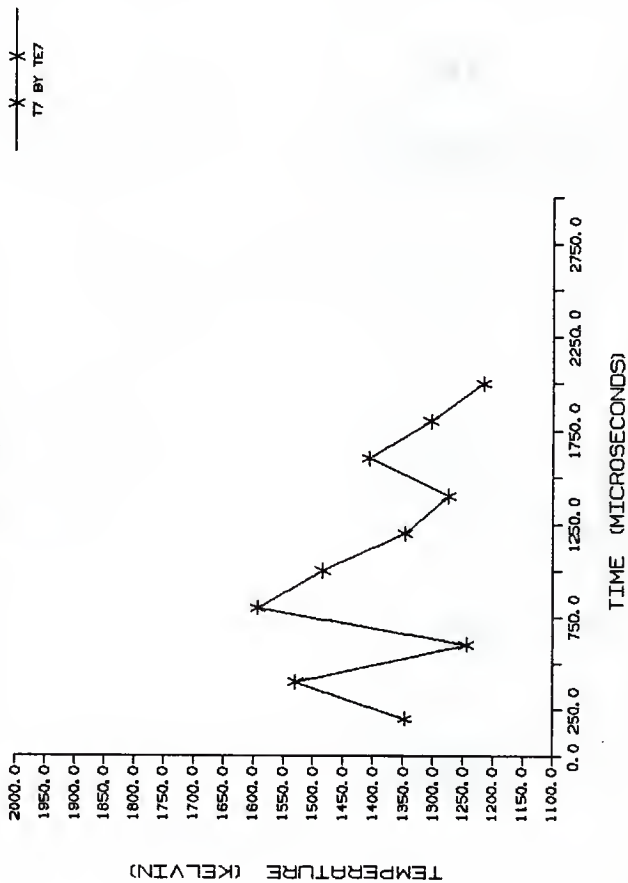


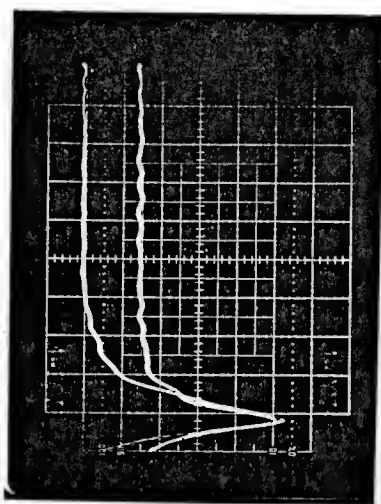
FIGURE 38a

Pyrometer output for a 33  $\mu\text{m}$  particle in air.

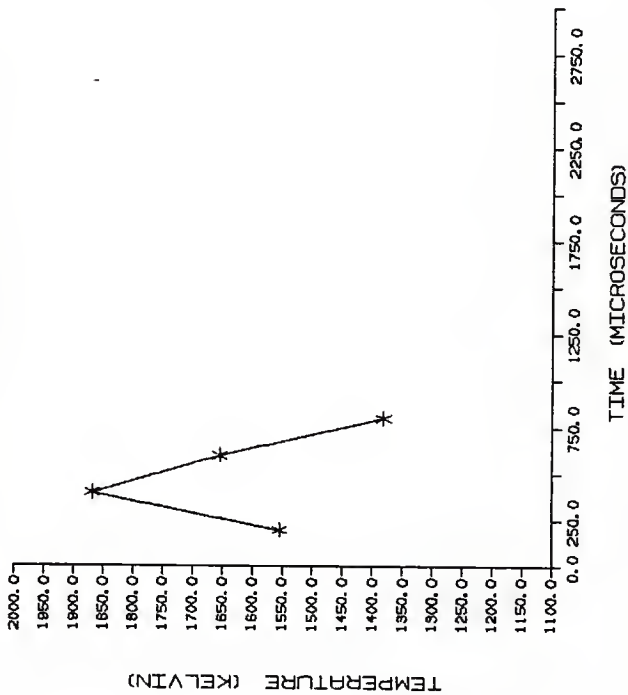
Laser Power        0.30 W  
Voltage Scale      100 mV/div.

FIGURE 38b

Time-temperature profile for the above.



TEMPERATURE PROFILE OF A  
GRAPHITE PARTICLE BURNING  
IN AIR



X X  
— BY TES

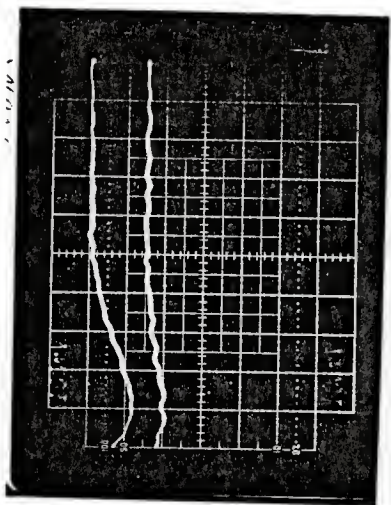
FIGURE 39a

Pyrometer output for a 22  $\mu\text{m}$  particle in air.

Laser Power        0.25W  
Voltage Scale      100mv/div.

FIGURE 39b

Time-temperature profile for the above.



TEMPERATURE PROFILE OF A  
GRAPHITE PARTICLE BURNING  
IN AIR

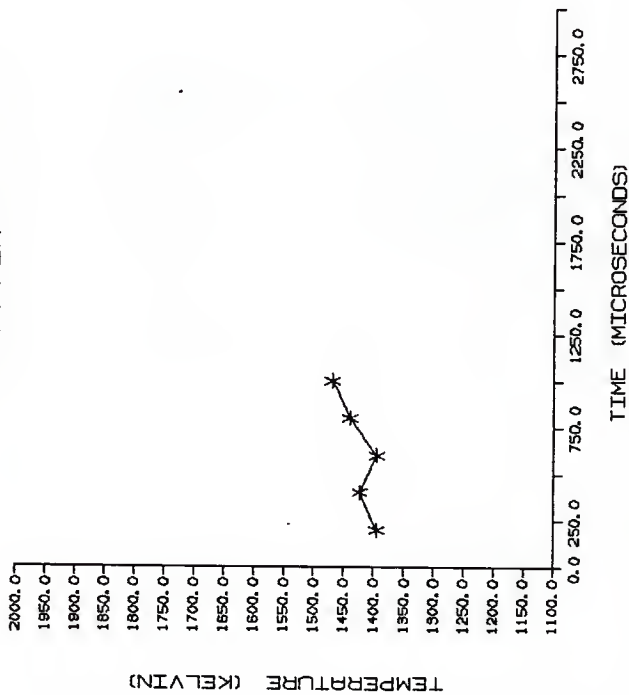


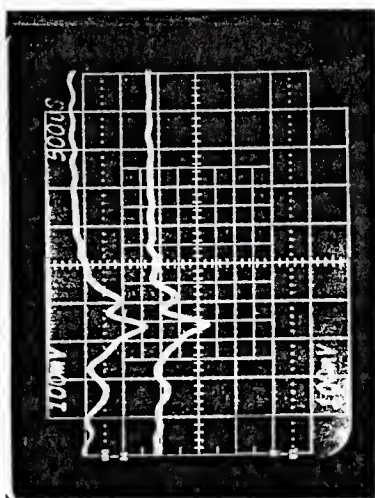
FIGURE 40a

Pyrometer output for a 25  $\mu\text{m}$  particle in air.

Laser Power      0.18W.

FIGURE 40b

Time-temperature profile for the above.



TEMPERATURE PROFILE OF A  
GRAPHITE PARTICLE BURNING  
IN AIR

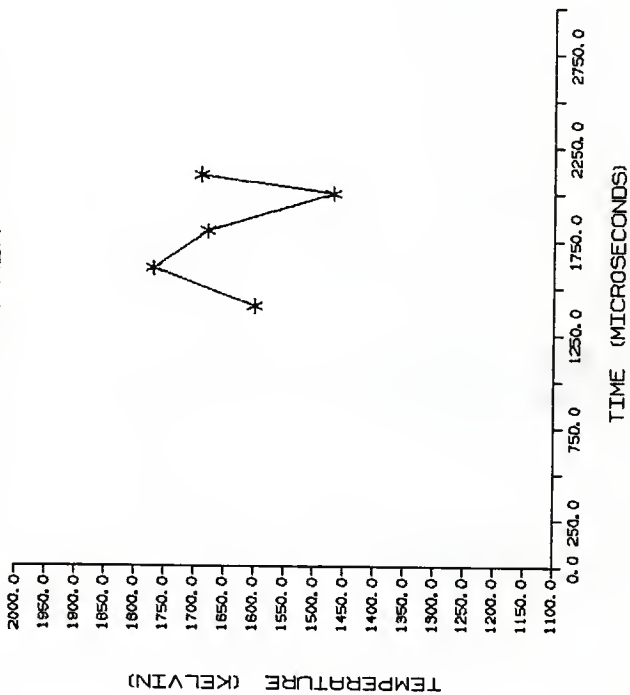
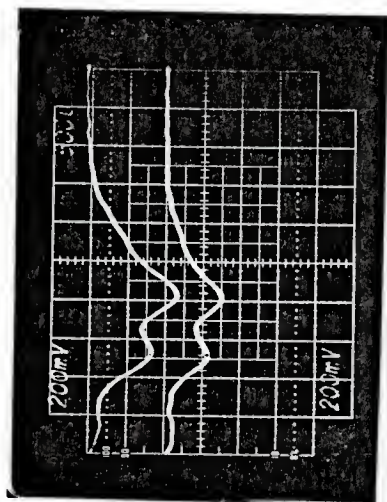


FIGURE 41a

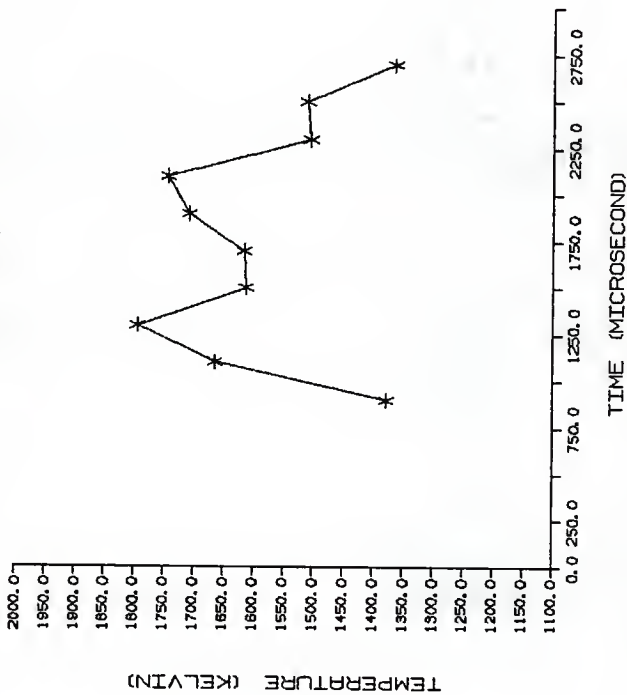
Pyrometer output for a "rotating" particle in air.

FIGURE 41b

Time-temperature profile for the above.



TEMPERATURE PROFILE OF A  
GRAPHITE PARTICLE BURNING  
IN AIR



— \* — \*  
T11 BY TE11

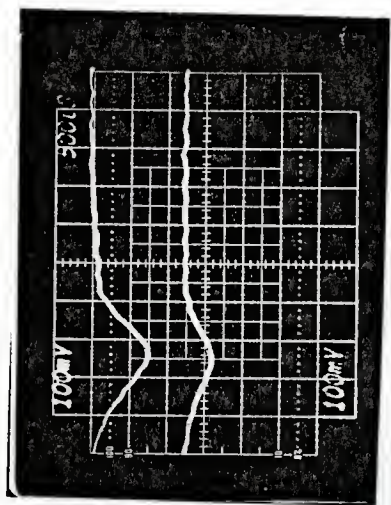
FIGURE 42a

Pyrometer output for a 30  $\mu\text{m}$  particle in nitrogen.

Laser Power            0.30W.

FIGURE 42b

Time-temperature profile for the above.



TEMPERATURE PROFILE OF  
A GRAPHITE PARTICLE  
IN NITROGEN

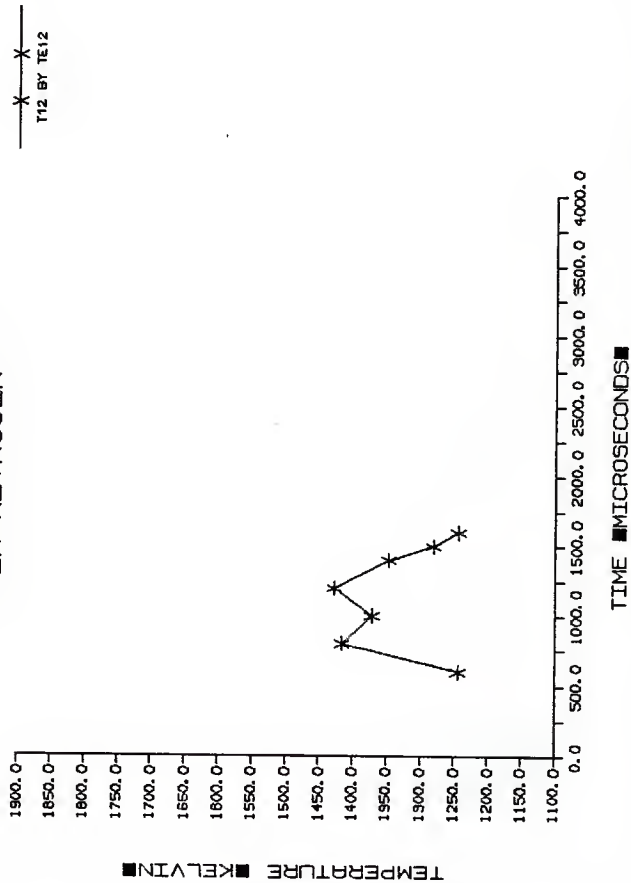
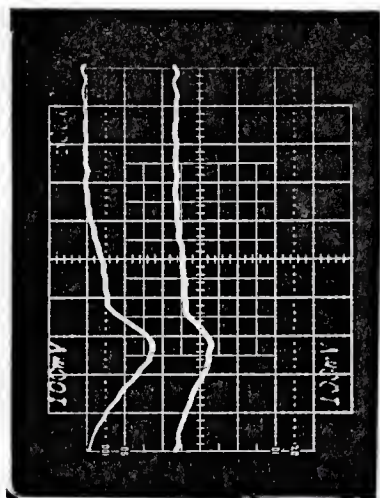


FIGURE 43a

Previous particle heated again.

FIGURE 43b

Time-temperature profile for the above.



TEMPERATURE PROFILE OF  
A GRAPHITE PARTICLE  
IN NITROGEN

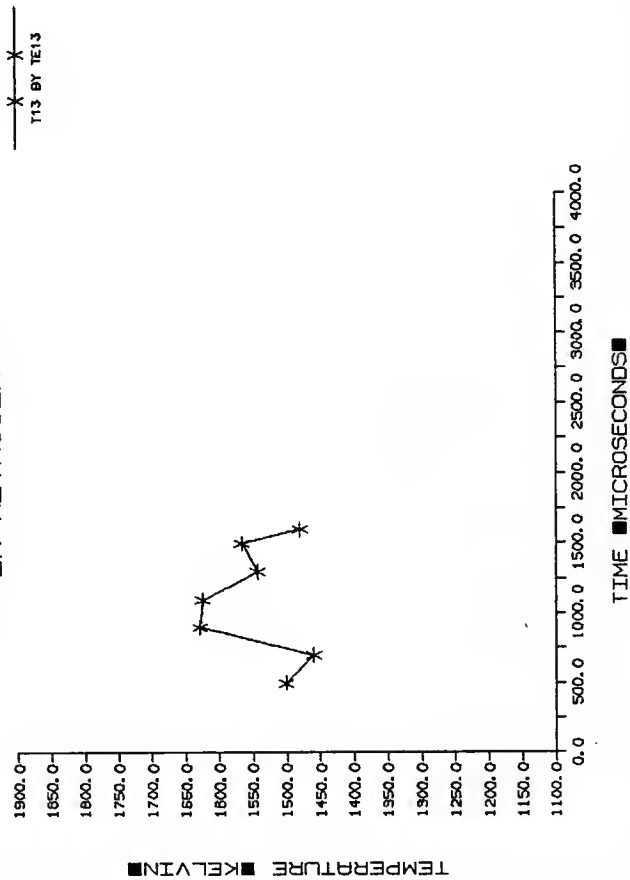


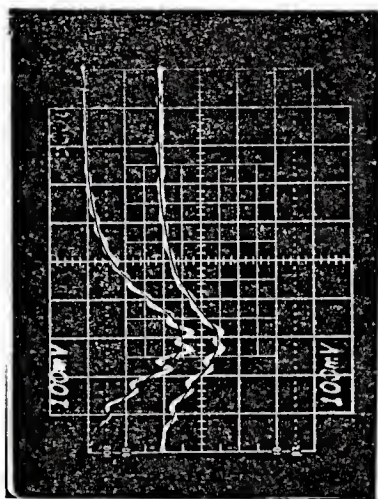
FIGURE 44a

Pyrometer output for a 27  $\mu\text{m}$  particle in nitrogen.

Laser Power            0.30W

FIGURE 44b

Time-temperature profile for the above.



TEMPERATURE PROFILE OF  
A GRAPHITE PARTICLE  
IN NITROGEN

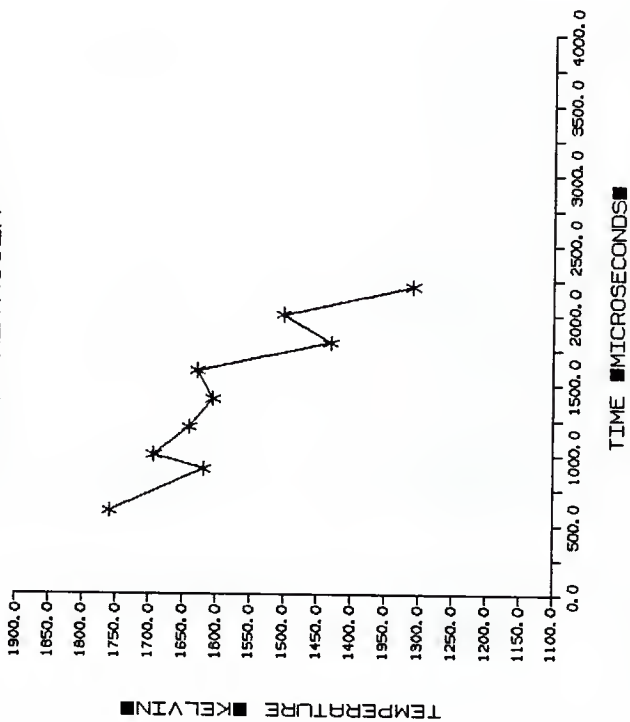


FIGURE 45a

Pyrometer output for a 30  $\mu\text{m}$  particle in nitrogen.

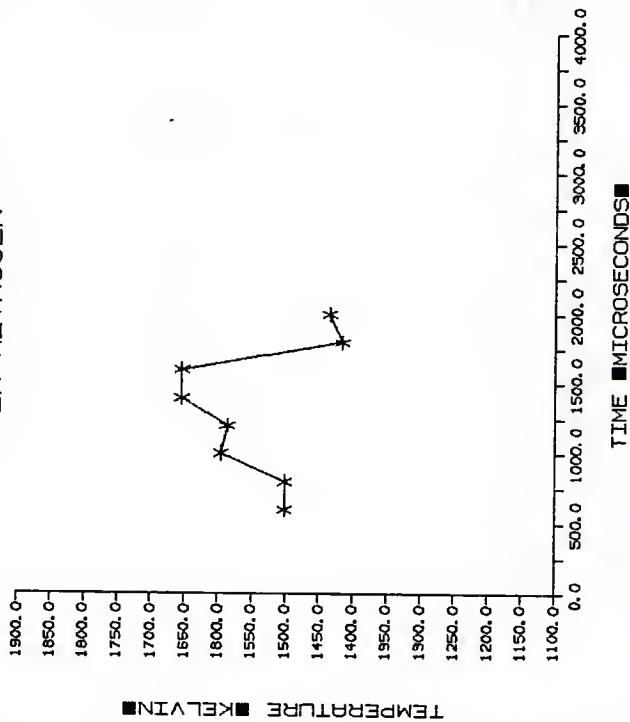
Laser Power            0.30W

FIGURE 45b

Time-temperature profile for the above.



TEMPERATURE PROFILE OF  
A GRAPHITE PARTICLE  
IN NITROGEN



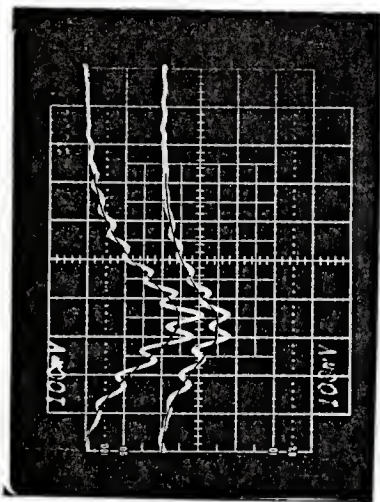
— X — X —  
T16 BY TE16

FIGURE 46a

Pyrometer output for a the particle in Fig. (45) heated again.

FIGURE 46b

Time-temperature profile for the above.



TEMPERATURE PROFILE OF  
A GRAPHITE PARTICLE  
IN NITROGEN

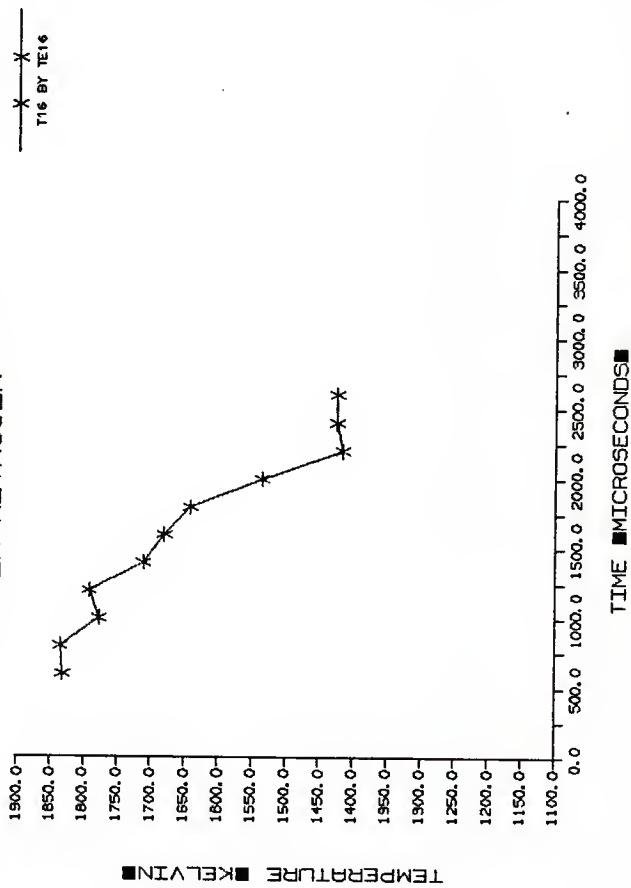
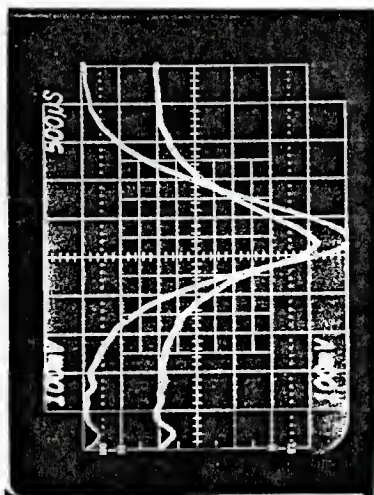


FIGURE 47a

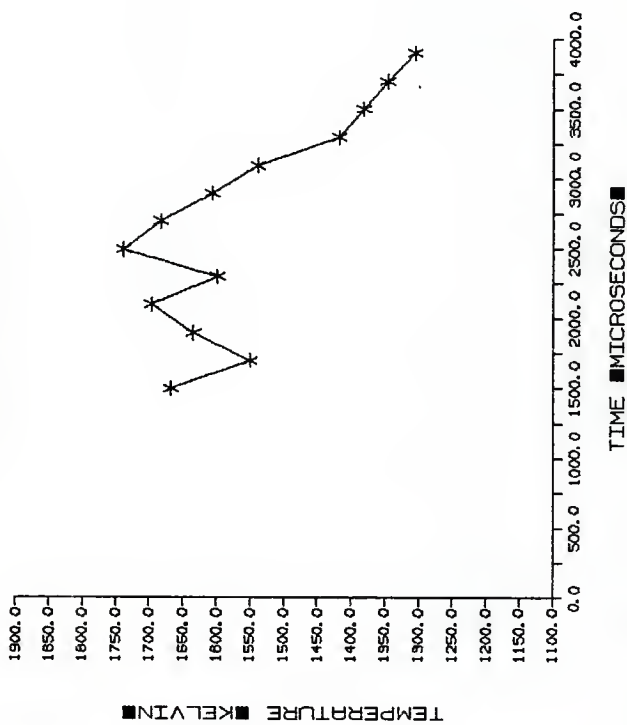
Pyrometer output for a 25  $\mu\text{m}$  particle in nitrogen.

FIGURE 47b

Time-temperature profile for the above.



TEMPERATURE PROFILE OF  
A GRAPHITE PARTICLE  
IN NITROGEN



— X — X — X  
T17 BY TE17

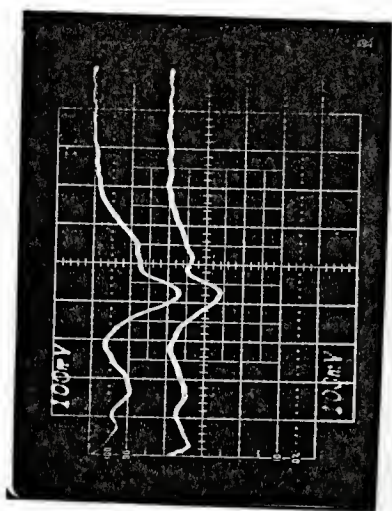
FIGURE 48a

Pyrometer output for a 25  $\mu\text{m}$  particle in nitrogen.

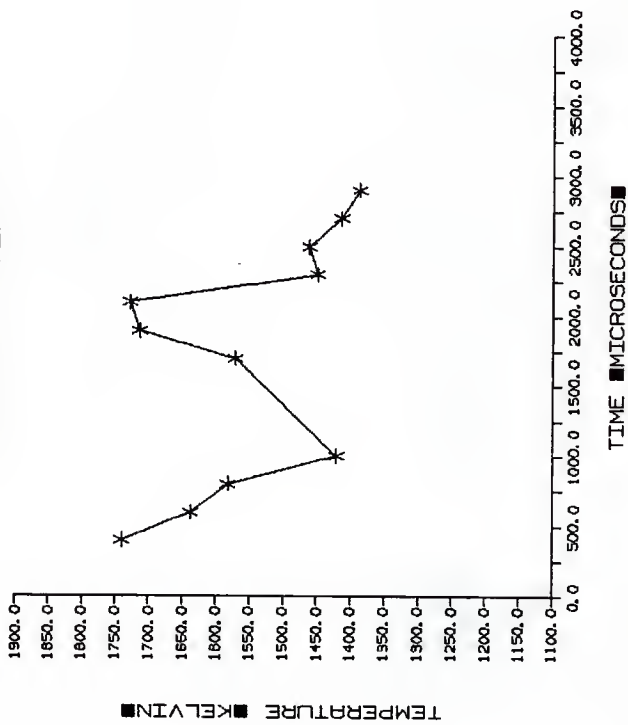
Laser Power            0.32W

FIGURE 48b

Time-temperature profile for the above.



TEMPERATURE PROFILE OF  
A GRAPHITE PARTICLE  
IN NITROGEN



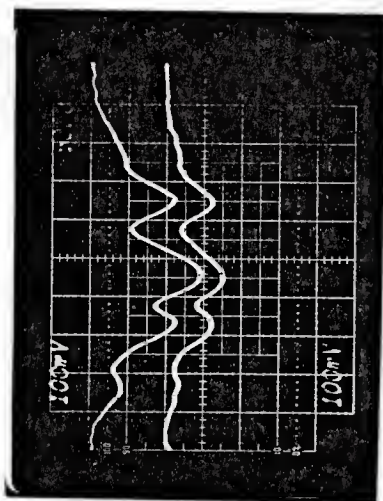
— X — X — X  
T161 BY TE18H

FIGURE 49a

Particle in Fig. (48) heated again.

FIGURE 49b

Time-temperature profile for the above.



TEMPERATURE PROFILE OF  
A GRAPHITE PARTICLE  
IN NITROGEN

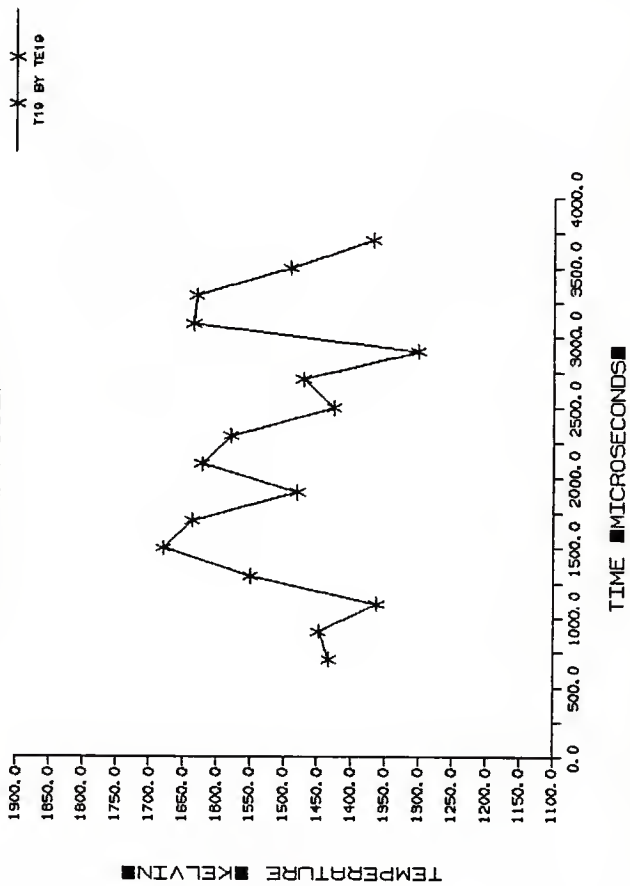


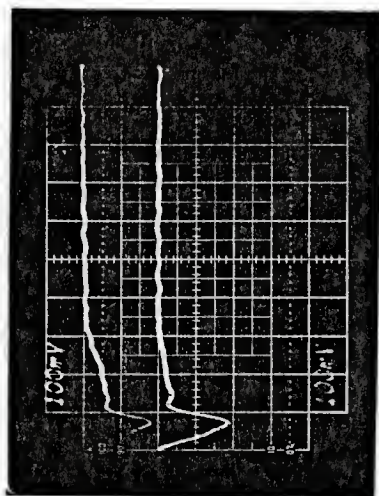
FIGURE 50a

Pyrometer output for a 27  $\mu\text{m}$  particle in oxygen.

Laser Power            0.34 W

FIGURE 50b

Time-temperature profile for the above.



TEMPERATURE PROFILE OF A  
GRAPHITE PARTICLE BURNING  
IN OXYGEN

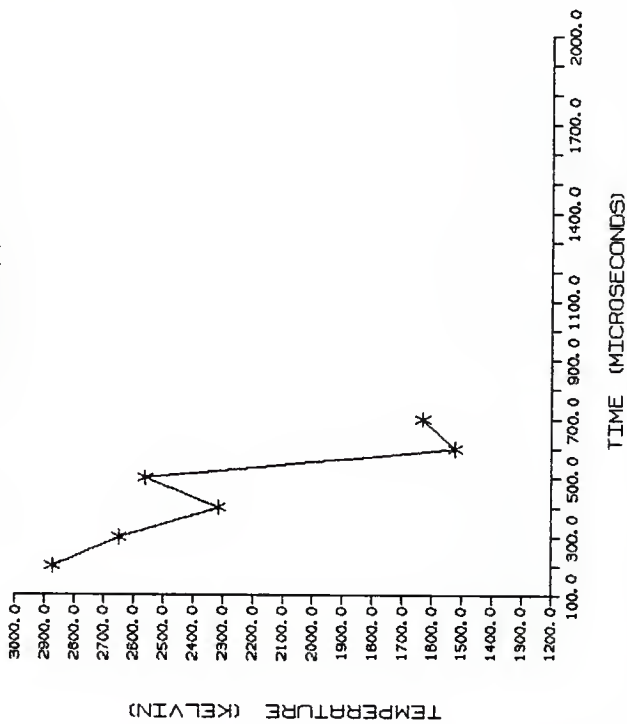


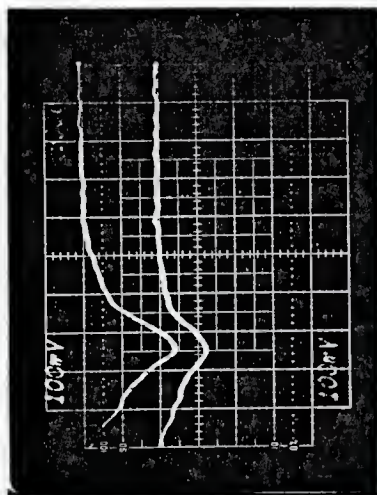
FIGURE 51a

Pyrometer output for a 35  $\mu\text{m}$  particle in oxygen.

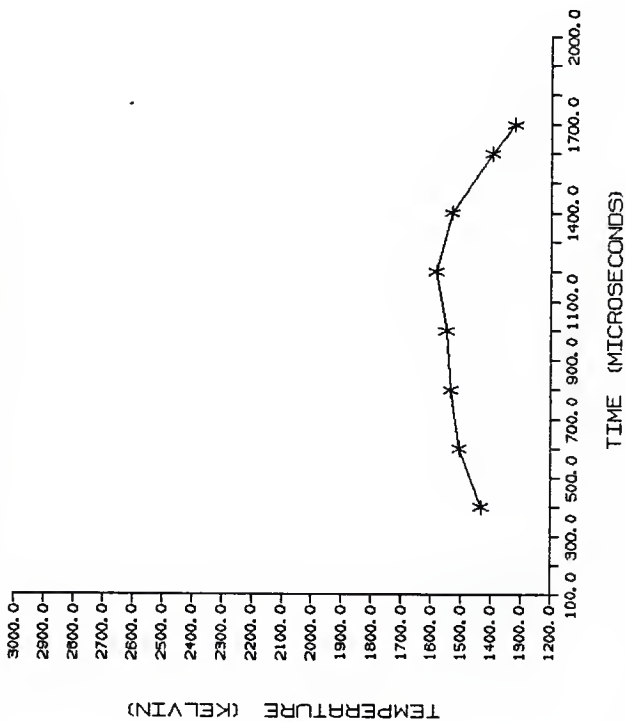
Laser Power            0.34 W

FIGURE 51b

Time-temperature profile for the above.



TEMPERATURE PROFILE OF A  
GRAPHITE PARTICLE BURNING  
IN OXYGEN



X X  
T21 BY TE21

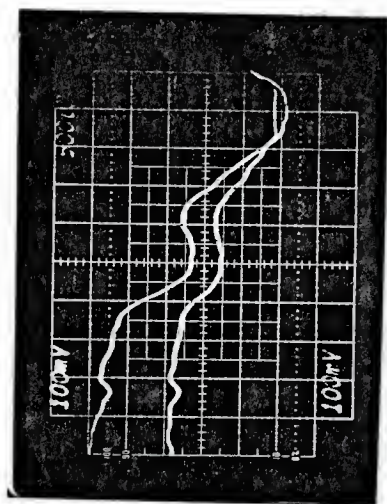
FIGURE 52a

Pyrometer output for a 30  $\mu\text{m}$  particle in oxygen.

Laser Power            0.34 W

FIGURE 52b

Time-temperature profile for the above.



TEMPERATURE PROFILE OF A  
GRAPHITE PARTICLE BURNING  
IN OXYGEN

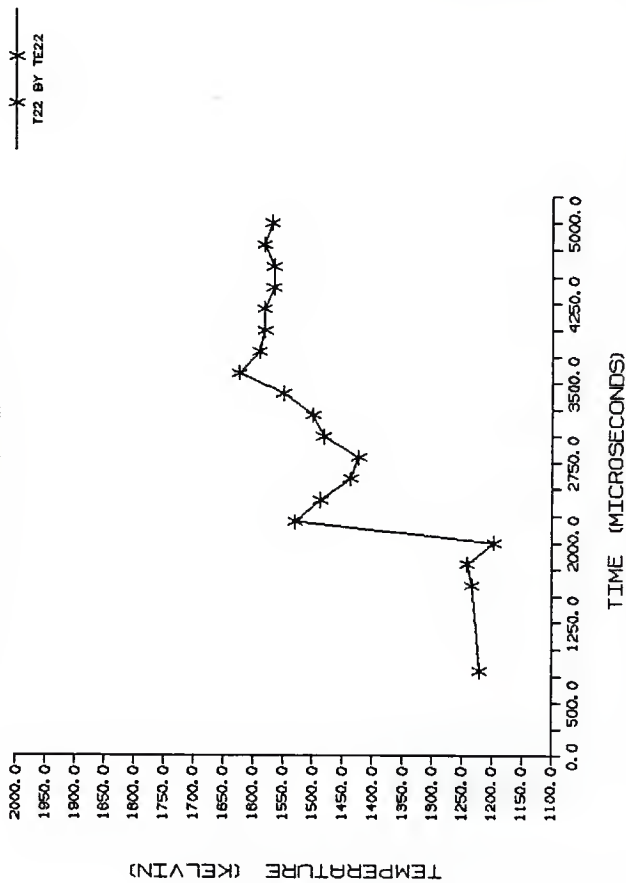


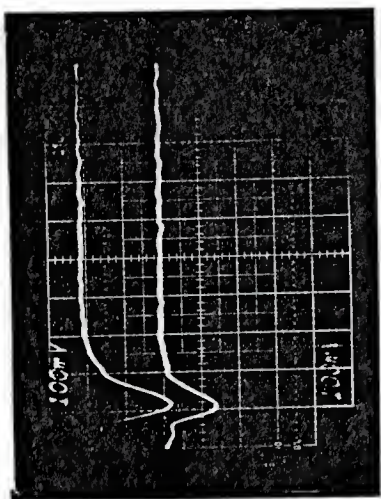
FIGURE 53a

Pyrometer output for a 17  $\mu\text{m}$  particle in oxygen.

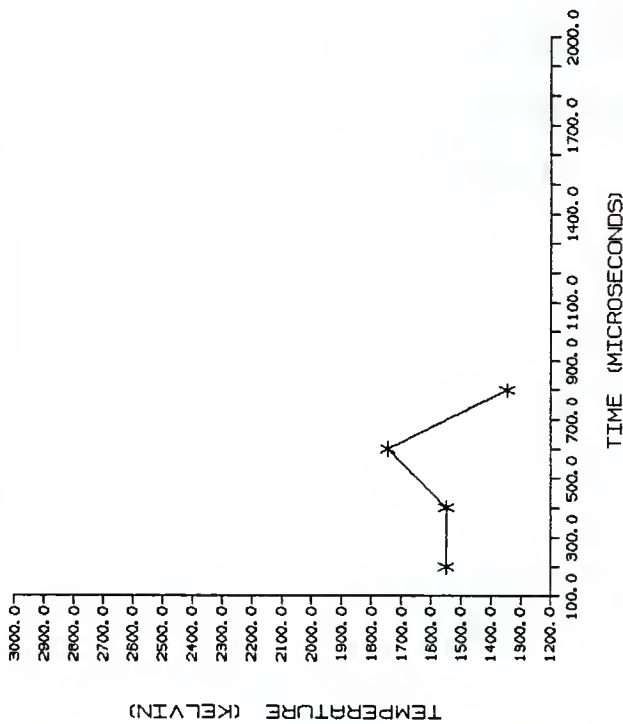
Laser Power            0.34 W

FIGURE 53b

Time-temperature profile for the above.



# TEMPERATURE PROFILE OF A GRAPHITE PARTICLE BURNING IN OXYGEN



X X  
T23 BY TE23

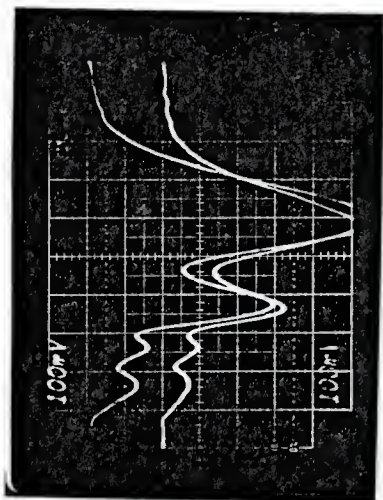
FIGURE 54a

Pyrometer output for a 27  $\mu\text{m}$  particle in oxygen.

Laser Power            0.34 W

FIGURE 54b

Time-temperature profile for the above.



TEMPERATURE PROFILE OF A  
GRAPHITE PARTICLE BURNING  
IN OXYGEN

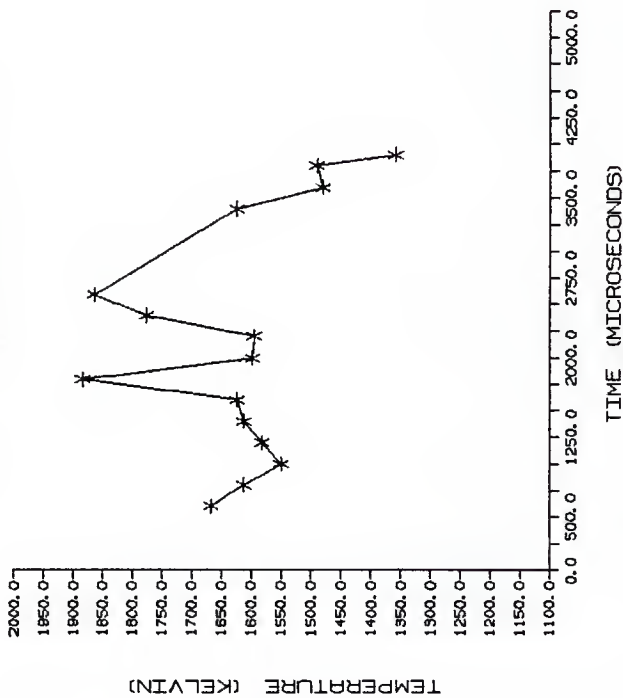


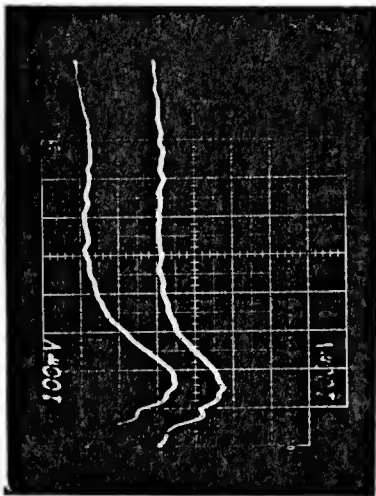
FIGURE 55a

Pyrometer output for a 15  $\mu\text{m}$  particle in oxygen.

Laser Power            0.34 W

FIGURE 55b

Time-temperature profile for the above.



TEMPERATURE PROFILE OF A  
GRAPHITE PARTICLE BURNING  
IN OXYGEN

— \* — \* —  
128 BY TE26

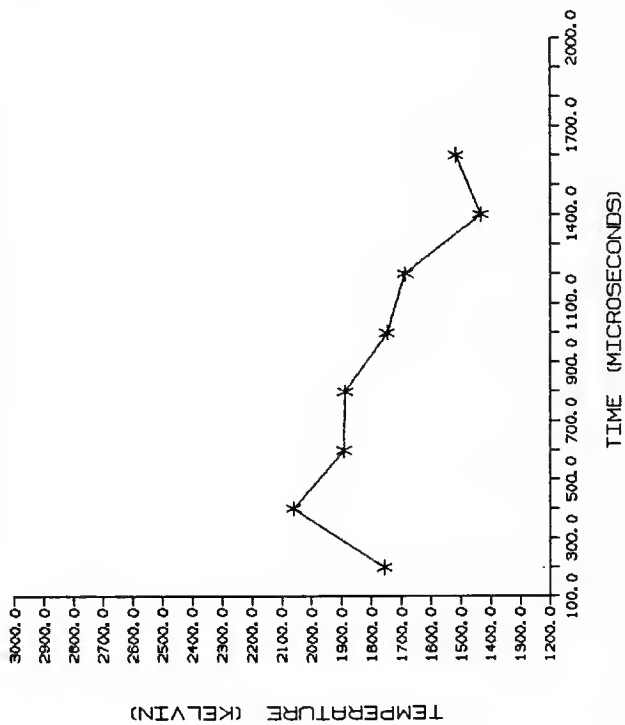


FIGURE 56a

Pyrometer output for a 30  $\mu\text{m}$  particle in oxygen.

Laser Power            0.34 W

FIGURE 56b

Time-temperature profile for the above.



TEMPERATURE PROFILE OF A  
GRAPHITE PARTICLE BURNING  
IN OXYGEN

X X  
126 BY 1E26

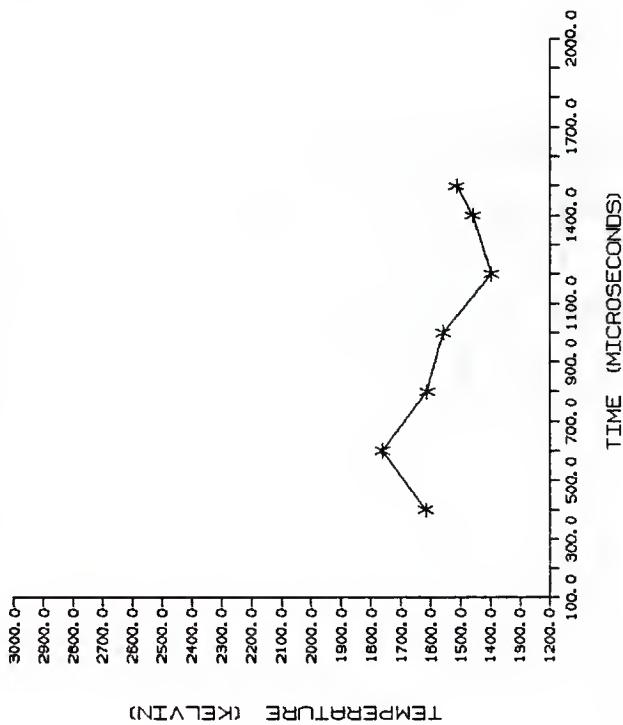


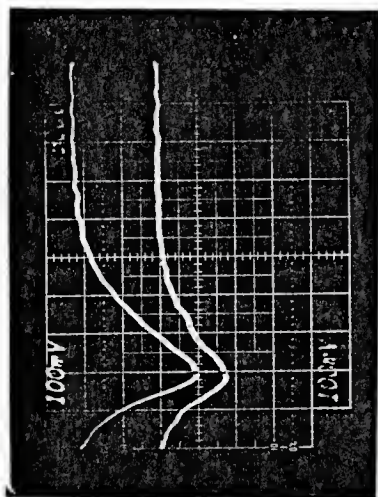
FIGURE 57a

Pyrometer output for a 30  $\mu\text{m}$  particle in oxygen.

Laser Power            0.32 W

FIGURE 57b

Time-temperature profile for the above.



TEMPERATURE PROFILE OF A  
GRAPHITE PARTICLE BURNING  
IN OXYGEN

X X X  
127 BY TE27

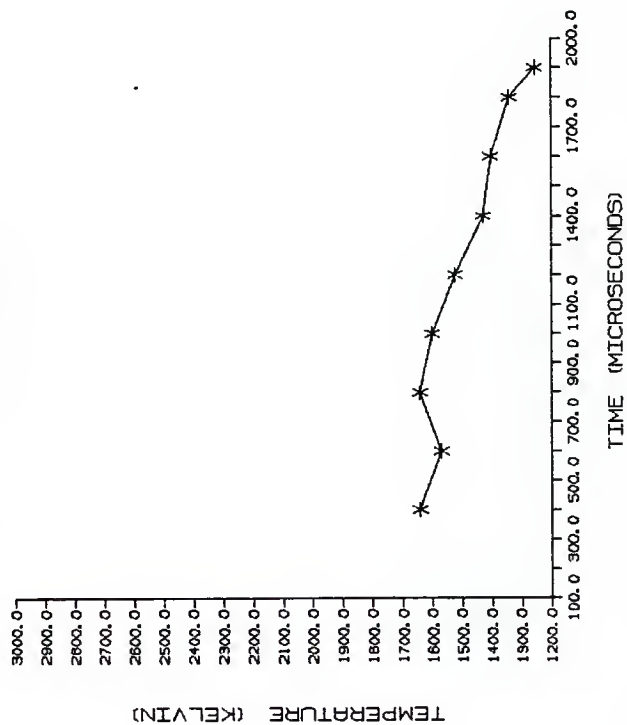
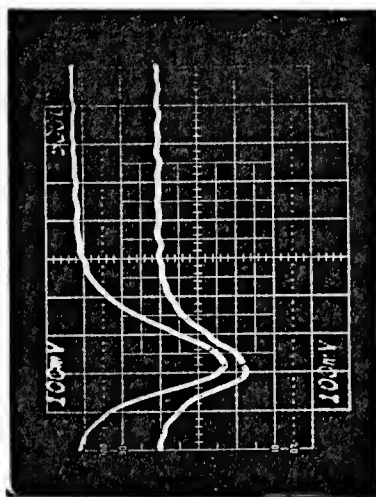
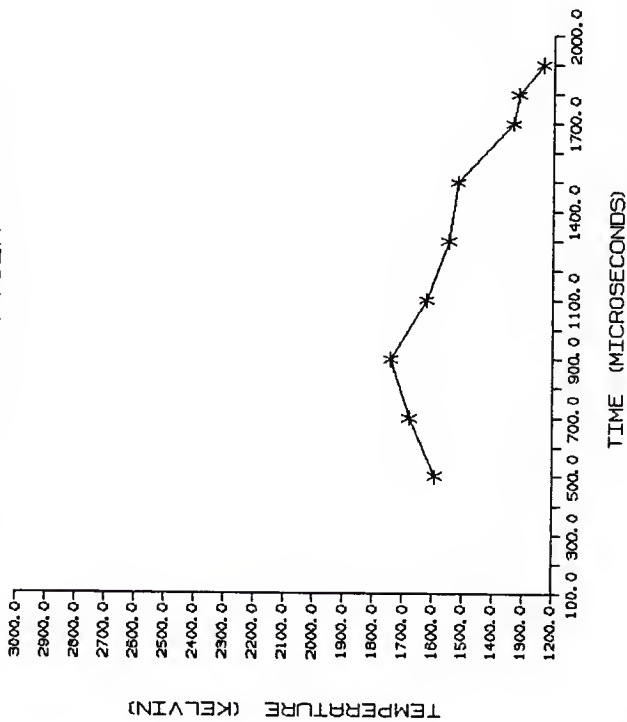


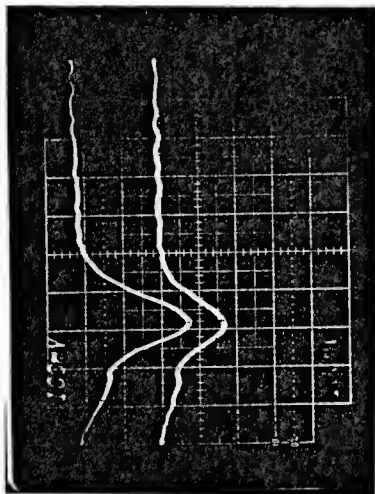
FIGURE 58

Particle in Fig. 57 heated again.

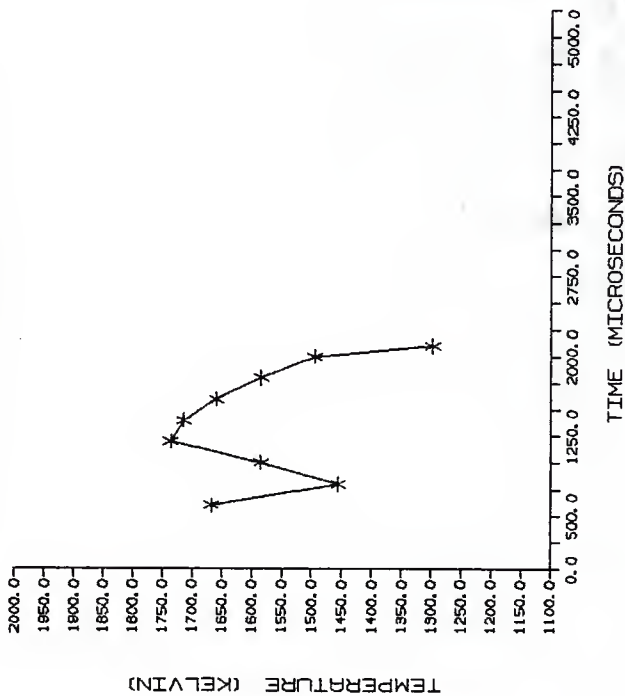


TEMPERATURE PROFILE OF A  
GRAPHITE PARTICLE BURNING  
IN OXYGEN





TEMPERATURE PROFILE OF A  
GRAPHITE PARTICLE BURNING  
IN OXYGEN



X X  
-----  
T29 BY TE29

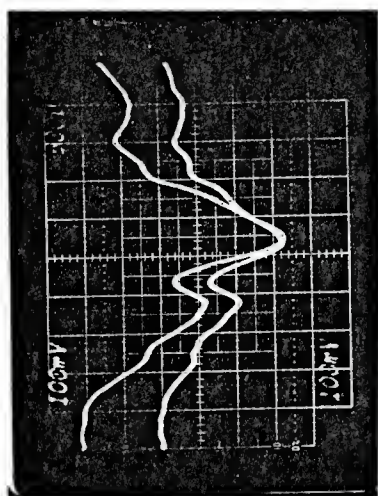
FIGURE 59a

Pyrometer output for a 34  $\mu\text{m}$  particle in oxygen.

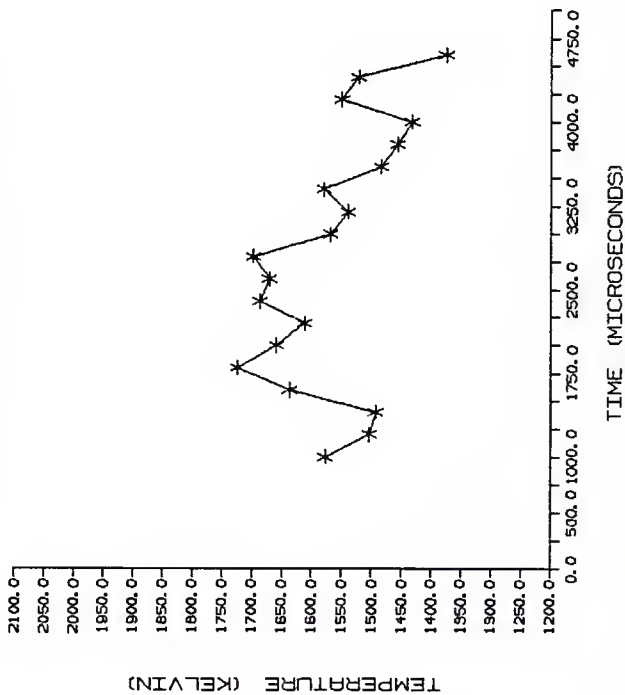
Laser Power            0.32W

FIGURE 59b

Time-temperature profile for the above.



TEMPERATURE PROFILE OF A  
GRAPHITE PARTICLE BURNING  
IN OXYGEN



## REFERENCES

1. Joseph Cerv, M.S. Thesis, Department of Nuclear Engineering, Kansas State University (1985).
2. W.Z. Nusselt, Ver Deut. Ing. 68, 124 (1924).
3. D.B. Spalding, Fuel 30, 121 (1951).
4. Coffin, K.P. and Brokaw, R.S., Tech. Note 3929 (1957).
5. Libby, P.A. and Blake, T.R., Comb. Flame 36, 139 (1979).
6. Laurendeau, N.M., Prog. Energy Comb. Sci. 4, 221 (1978).
7. Hottel, H.C. and Davis, H., Ind. Eng. Chem. 26, 889 (1934).
8. Ubhayaker, S.R. and Williams, F.A., Electrochem. Soc. 123, 747 (1976).
9. Frickel, R.H., Shaffer, R.E. and Stamatoff, J.B., "Chambers for the electrodynamic containment of charged aerosol particles", Chemical Systems Laboratory, Aberdeen Proving Ground, MD 21010 (1970).
10. Arnold, S., J. Aerosol Sci. 10, 49 (1979).
11. Philip, M.A., Gelbard, F. and Arnold, S., J. Coll. Int. Sci., 41, 507 (1983).
12. Hottel, H.C. and Broughton, F.P., Ind. Eng. Chem., 4 (1932): 166-174.
13. House, K., B.S. Thesis, MIT, Dept. of Chemical Engineering (1978).
14. Dictor, R.A., M.S. Thesis, MIT, Dept. of Chemical Engineering (1979).
15. Quinn, T.J., Temperature, 7, 294 (1983).
16. Ayling, A.B. and Smith, I.W., Comb. Flame 18, 173-84 (1972).
17. Wolfe, W.L. and Zissis, G.J., The Infrared Handbook, 2, 12 (1978).

TWO-COLOR PYROMETER TEMPERATURE PROFILES FOR  
SINGLE PARTICLE GRAPHITE COMBUSTION

by

Upendra Brahme

---

AN ABSTRACT OF A MASTER'S THESIS

submitted in partial fulfillment of the  
requirement for the degree

MASTER OF SCIENCE

Department of Physics  
KANSAS STATE UNIVERSITY  
Manhattan, Kansas

1986

82-21  
000

## ABSTRACT

Experimental data on the temperature-time profile of laser heated particles of AESAR crystalline graphite with diameters in the range 15 to 50  $\mu\text{m}$  in ambient environments of nitrogen, air and oxygen are presented. The modified Millikan cell was used to suspend individual graphite particles. The temperature-time measurements were made with a two-color pyrometer. Intensity traces were recorded to determine particle temperature histories and possible "burning" times.

Correlation between "burning" time and particle size indicated that larger particles "burned" longer and had lower peak temperatures. Ambient environment had no significant effect on the particle peak temperatures. Typical peak temperatures ranged from 1700 to 2200<sup>o</sup>K while the "burning" times ranged from 2 to 5 ms. Particles ignited by the laser more than once achieved more or less the same temperature. These results led the author to conclude that particles in the range of 15 to 50  $\mu\text{m}$  could not sustain combustion.